nature metabolism

Article

https://doi.org/10.1038/s42255-023-00962-0

Readily releasable β cells with tight Ca^{2+}–exocytosis coupling dictate biphasic glucose-stimulated insulin secretion

Received: 23 May 2022

Accepted: 5 December 2023

Published online: 26 January 2024

Check for updates

Xiaohong Peng[1,2,3,14], Huixia Ren[1,4,14], Lu Yang[1,5,14], Shiyan Tong[1,6,14], Renjie Zhou[1], Haochen Long[7], Yunxiang Wu[1], Lifen Wang[8], Yi Wu[1], Yongdeng Zhang[9], Jiayu Shen[1], Junwei Zhang[1], Guohua Qiu[1], Jianyong Wang[1], Chengsheng Han[1], Yulin Zhang[1], Mengxuan Zhou[1], Yiwen Zhao[1], Tao Xu[10,11], Chao Tang[4], Zhixing Chen[12], Huisheng Liu[3,10,11] ✉ & Liangyi Chen[1,13] ✉

Biphasic glucose-stimulated insulin secretion (GSIS) is essential for blood glucose regulation, but a mechanistic model incorporating the recently identified islet β cell heterogeneity remains elusive. Here, we show that insulin secretion is spatially and dynamically heterogeneous across the islet. Using a zinc-based fluorophore with spinning-disc confocal microscopy, we reveal that approximately 40% of islet cells, which we call readily releasable β cells (RRβs), are responsible for 80% of insulin exocytosis events. Although glucose up to 18.2 mM fully mobilized RRβs to release insulin synchronously (first phase), even higher glucose concentrations enhanced the sustained secretion from these cells (second phase). Release-incompetent β cells show similarities to RRβs in glucose-evoked Ca^{2+} transients but exhibit Ca^{2+}–exocytosis coupling deficiency. A decreased number of RRβs and their altered secretory ability are associated with impaired GSIS progression in *ob*/*ob* mice. Our data reveal functional heterogeneity at the level of exocytosis among β cells and identify RRβs as a subpopulation of β cells that make a disproportionally large contribution to biphasic GSIS from mouse islets.

Glucose-stimulated insulin secretion (GSIS) from pancreatic β cells facilitates the downstream absorption and utilization of glucose, and these effects maintain tight glucose homoeostasis in the circulation. A stepwise increase in blood glucose levels evokes biphasic insulin secretion consisting of a fast first phase and a sustained second phase. A defect in the first phase represents an early sign of β cell dysfunction in type 2 diabetes[1,2], and its restoration by gastric bypass surgery leads to immediate improvements in glucose tolerance without weight reduction or sensitized insulin function[3]. Therefore, the transient first phase is indispensable to tight glucose homoeostasis in vivo, but the underlying molecular mechanism is unclear.

The prevailing model suggests the existence of distinct pools of secretory vesicles in β cells; the depletion of the readily releasable pool (RRP) accounts for the fast first phase, whereas its replenishment confers the slow phase[4]. Although this vesicle-centric model has received much support[5–7], it does not take into account the β cell heterogeneity found in dissociated β cells[8,9] and intact islets[10,11]. In fact, β cells can be categorized into subpopulations based on the expression of protein markers[12], single-cell omics[13], and functional heterogeneity in terms of glucose metabolism (nicotinamide adenine dinucleotide phosphate response, glucokinase expression)[14,15] and glucose-stimulated Ca^{2+} signalling in the islet[16,17]. In addition, β cells reside in environmental niches containing other cell types[18–21]. How different subpopulations of β cells interact with each other and with other cell types in the islet to shape the stimulation–secretion coupling remains unknown, and the major challenge lies in detecting insulin secretion originating from different islet β cells.

A full list of affiliations appears at the end of the paper. ✉e-mail: liu_huisheng@grmh-gdl.cn; lychen@pku.edu.cn

https://doi.org/10.1038/s42255-023-00962-0

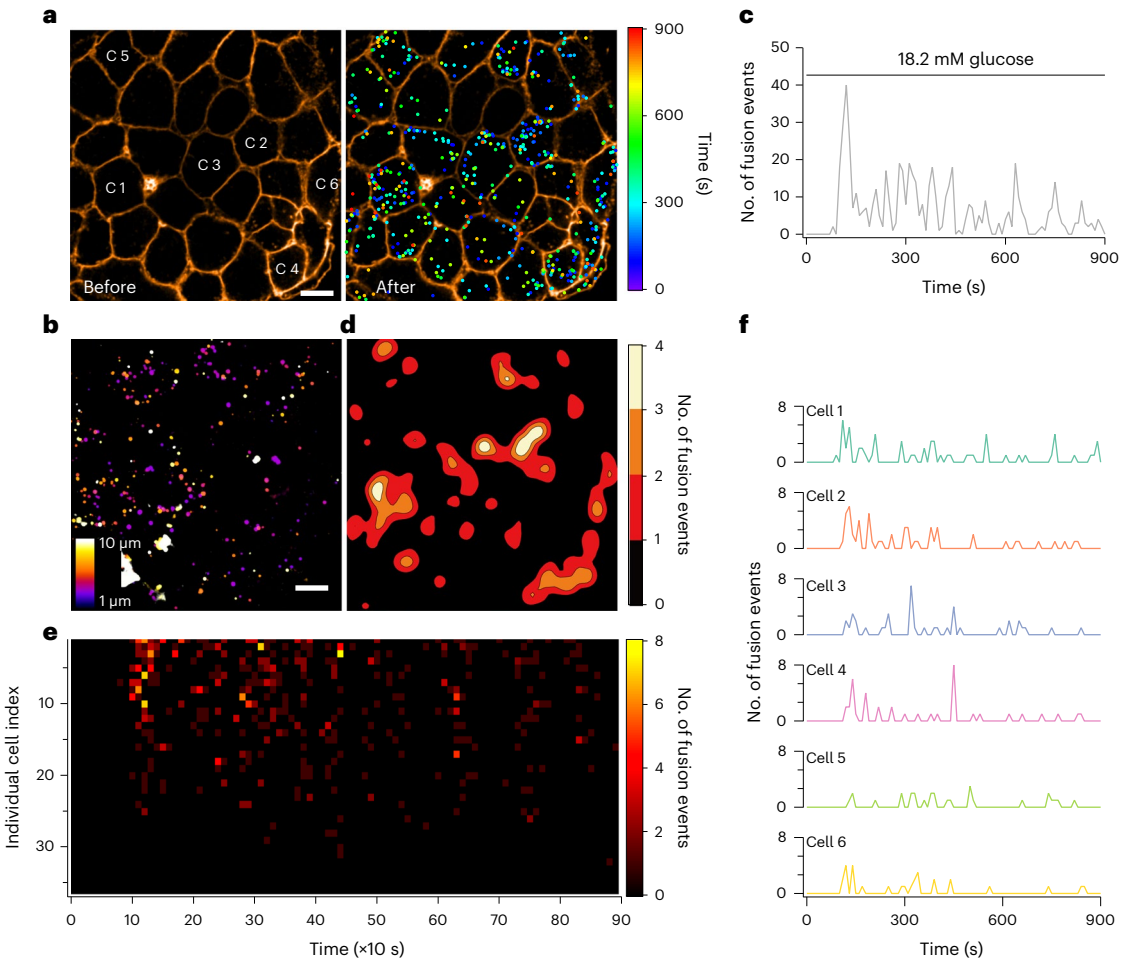

Fig. 1 | Glucose stimulates spatially and dynamically heterogeneous insulin secretion within an intact islet. a, Exocytosis in an islet (from a male mouse) before (left) and after (right) glucose (18.2 mM) stimulation. Colour-coded puncta represent fusion sites and time. The plasma membrane was labelled with FM 4-64 dye (orange). C1–C6 marks six cells with the highest secretion. **b**, Three-dimensional distribution of fusion events labelled with FluoZin-1 in an islet (from a male mouse). The *z* axis is colour-coded. **c**, Time-dependent histogram of glucose-induced fusion events in the whole islet shown in **a**. The time point '0 s' indicates the start of glucose stimulation. **d**, Heatmap of the fusion event density in the islet shown in **a**. **e**, Time-dependent heatmap of exocytosis from individual cells in the islet shown in **a**. The rows represent cells ranked by secretory capacity (number of fusion events in 15 min). Each pixel represents the colour-coded fusion events occurring within 10 s. **f**, Exocytosis frequency histograms of glucose-induced fusion events from the top 6 cells shown in **e**. Their positions are highlighted in **a**. Representative images represent at least three biological replicates (**a**, **b**). Scale bar = 10 µm.

We visualized hundreds of glucose-stimulated vesicular exocytotic events in intact mouse islets in situ by combining the use of a zinc-based fluorophore with spinning-disc confocal microscopy. We found an exponential distribution of the secretory capacity of β cells within the islet, which was modulated by the paracrine input from neighbouring cells, including δ cells. In contrast, the synchronous and asynchronous release from the same readily releasable β cells (RRβs) dominates the biphasic GSIS. This individual-cell-centric mechanism demonstrates the critical dysfunction in biphasic GSIS at the islet level during the progression of diabetes in *ob*/*ob* mice.

Results

Spatially and temporally heterogeneous secretion in the islet

Two-photon microscopy combined with the use of non-cell-permeable fluorescent probes allows for the visualization of individual secretion events within islets[22,23]. However, this approach cannot distinguish whether the release occurs from insulin-, glucagon- or somatostatin (SST)-containing vesicles and cannot separate exocytosis from endocytosis. We used a non-cell-permeable fluorescent Zn^{2+} indicator, FluoZin-1, to detect the zinc coreleased with insulin within islets[24] under a spinning-disc confocal microscope (Extended Data Fig. 1a). The stimulation of an intact islet with an extracellular solution containing 18.2 mM glucose and FluoZin-1 (8 µM) resulted in the abrupt (1–2 min later) emergence of fluorescent puncta, which represent the individual fusion of insulin granules from β cells (named 'zinc flickers'; Fig. 1a, Extended Data Fig. 1b and Supplementary Video 1). The inclusion of FluoZin-1 did not affect insulin secretion, as demonstrated by conventional ELISA (Extended Data Fig. 1c). Moreover, exocytosis labelled with FluoZin-1 could be observed in deep layers of the islet, suggesting that FluoZin-1 and glucose readily diffused through the interstitial space to reach cells in the islet core (Fig. 1b). Preincubating islets with 250 µM diazoxide repolarized β cells and almost abolished zinc flickers (Extended Data Fig. 1d,e), whereas removing diazoxide re-evoked zinc flickers (Extended Data Fig. 1f). Moreover, zinc flickers seldom occurred within α or δ cells (indicated by glucagon-Cre-driven GCaMP6f expression (*Glu-GCaMP* mice) and SST-Cre-driven tdTomato expression (*Stdt* mice), respectively; Extended Data Fig. 1g–i). Therefore, the 'zinc flicker' method is a sensitive and specific approach for detecting insulin granule secretion.

To follow the time-dependent exocytosis process, we focused on a plane above the glass coverslip (superficial layer of the islet) and continuously imaged this plane at 3–5 Hz for >15 min. The ensemble

secretion showed a rapid peak followed by multiple smaller peaks, resembling the biphasic GSIS measured by ELISA (Fig. 1c). By labelling the cell membrane within the islet with FM 4-64 (Fig. 1a), we appreciated the heterogeneous secretion from different β cells in situ. Spatial analysis revealed that fusion puncta clustered at 'hotspots', as manifested in three-dimensional stacks (Fig. 1b) or from time-lapse summations of secretions in one plane (Fig. 1d). The examination of individual β cells showed that, although many β cells remained silent most of the time, a few β cells secreted persistently (Fig. 1e). Instead of sharing the same biphasic kinetics, these hypersecretory cells released insulin concurrently during the onset of glucose stimulation and asynchronously later (Fig. 1e,f). Therefore, exocytosis evoked by glucose within intact islets exhibits spatial and temporal heterogeneity, indicating that biphasic GSIS should be dissected at the individual β cell and ensemble islet levels.

RRβs dictate biphasic GSIS

Following stimulation with increasing glucose concentrations, the first phase of GSIS in single islets (0–5 min after stimulation) progressed gradually. In contrast, the sustained second phase (5–15 min after stimulation) started to manifest at glucose concentrations >9.8 mM (Fig. 2a,b). These data agree with previous ELISA measurements conducted in perfused rat pancreas[25] and mouse islets[26]. The total secretion of the first peak evoked by 18.2 mM glucose approximated that stimulated by the sequential application of 9.8 and 18.2 mM glucose (366 ± 50 versus 460 ± 148 events) under the staircase stimulation; the secretion evoked by 29.2 mM glucose also approximated that produced by the sequential application of 9.8, 18.2 and 29.2 mM glucose (554 ± 112 versus 682 ± 231 events; Fig. 2b,c). These data support the package-storage hypothesis of insulin secretion[25] and show that glucose concentrations limit the amplitude of the first phase of GSIS.

Although increased glucose stimulation generally reduced the number of nonresponsive cells (Fig. 2d), responsive cells still exhibited variable responses (Extended Data Fig. 2a). To quantify this heterogeneity, we defined the total number of fusion events within a single cell (during 15 min of stimulation) as the secretory capacity (s), the number of responsive cells from all islets as N, the number of cells with a secretory capacity s as $n(s)$ and the number of cells with a secretory capacity larger than s as $N(s)$. Specifically, we found that the complementary cumulative distribution function (CCDF) of the secretory capacity followed the same exponential distribution, $N(s) = N \times \exp(-k \times s)$ (Fig. 2e, Extended Data Fig. 2 and Methods), whereas k varied at different glucose concentrations. By taking the derivative, the probability density distribution function was calculated as $n(s) = N \times k \times \exp(-k \times s)$, an exponential function indicating uneven contributions from different cells. We then introduced the Gini coefficient[27] to evaluate the heterogeneous contribution of different cells quantitatively (Fig. 2f and Methods). With increases in the glucose concentration, the Gini coefficient of all islet cells (including nonresponsive cells) decreased to 0.54 (Fig. 2g), which closely resembled the constant (0.5) for ideal exponential distributions. Therefore, despite a ~24.8-fold change in exocytosis (7 mM: 53 ± 9 fusion events versus 29.2 mM: 1,315 ± 225 fusion events), glucose constantly stimulated secretion from a select group of β cells within islets.

Thus, we termed highly secretory β cells that contributed to 80% of the total insulin secretion as RRβs. These cells comprised approximately 40% of all islet cells under stimulation with glucose concentrations >18.2 mM (Fig. 2h). Assuming that, on average, non-β, nonresponsive cells constituted 10% of islet cells (refer to 16% or 6% nonresponsive cells under 18.2 and 29.2 mM glucose stimulation, respectively, in Fig. 2d), it implies that almost half of the β cells within the islet were incapable of insulin secretion. Consequently, these β cells are referred to as release-incompetent β cells (RIβs). Although glucose mobilized the same pool of RRβs during both phases of GSIS (Fig. 2i), 18.2 mM glucose almost activated the secretion from all individual RRβs during the first phase (Fig. 2h) and accelerated vesicle exocytosis after stimulation (Fig. 2j). In contrast, higher glucose concentrations continuously enhanced sustained insulin secretion from individual RRβs (Fig. 2k), and this enhancement also contributed to the synchronized release that manifested as the potentiated second phase of secretion (Fig. 2l,m, Extended Data Fig. 3 and Methods). Under conditions in which the second phase of secretion was potentiated by 18.2 or 29.2 mM glucose, RRβs also largely contributed to the second phase of GSIS (Fig. 2n). By designing an islet perfusion system, we exposed the islet to repeated glucose stimulation (18.2 mM initially, then reverted to 3 mM, followed by another 18.2 mM; Extended Data Fig. 4a). Insulin secretion demonstrated spatiotemporal repeatability (Fig. 2o,p). The secretion capacity of β cells (labelled with GCaMP6f in the *Ins1-Cre*$^{+/-}$; *Ins-GCaMP* mouse line) showed a nearly linear correlation ($R^2 = 0.64$), with approximately 83% of RRβs and 86% of RIβs in the second round being the same as those in the first round (Fig. 2q,r). This spatiotemporal repeatability of insulin secretion and Ca^{2+} dynamics was similar in islets from female and male mice (Extended Data Fig. 4b–e). Collectively, these data affirm that RRβs constitute a distinct subpopulation. Therefore, glucose stimulation selectively activates RRβs within the islet and modulates the biphasic GSIS through efficient RRβ mobilization, synchronization and sustained exocytosis capabilities.

Tight coupling between Ca^{2+} and exocytosis in RRβs

To explore the differences between RRβs and RIβs, we simultaneously monitored the Ca^{2+} dynamics and insulin secretion in the same *Ins-GCaMP* islets using a red zinc-bound probe (PKZnR-1; Supplementary Video 2)[28]. Although different islet β cells exhibited varied secretion levels (Fig. 3a,b), their Ca^{2+} dynamics were similar, displaying a steady or oscillating second phase (Fig. 3c,d). By quantitatively analysing the maximum amplitude and initiation speed of Ca^{2+} transients in the first phase (Fig. 3e), we found that, despite the more than sevenfold larger exocytosis (Fig. 3f; steady: 33 ± 2 versus 5 ± 0.5 fusion events, oscillating:

Fig. 2 | RRβs orchestrate biphasic GSIS. a, Representative example images of exocytosis. Glucose concentration is shown in the upper-left corner of each image. Colour-coded puncta represent fusion sites and time. Orange pseudocolour marks the plasma membrane. **b**, Time-dependent fusion events induced by single-step or staircase glucose stimulation. **c**, Fusion events in the first phase (a1, b1, c1) of single-step or staircase stimulation. **d**, Ratio of nonresponsive cells. **e**, CCDF of the secretory capacity of total responsive cells. The R^2 values are 0.93 (7 mM glucose), 0.96 (9.8 mM glucose), 0.99 (18.2 mM glucose) and 0.98 (29.2 mM glucose). **f**, Gini coefficient is the ratio of the area that lies between the line of equality and Lorenz curve (marked A) over the total area above the line of equality (marked A and B). **g**, Gini coefficient statistics. **h**, Ratio of RRβs. **i**, Ratio of colocalization of RRβs between the first and second phase. **j**, Delay time in RRβs. Centre line, median; limits, 75% and 25%; whiskers, maximum and minimum. **k**, Secretory capacity of RRβs in different phases. **l**, Synchronization of RRβs at 10-s intervals. **m**, Synchronization ratio in different phases of GSIS. **n**, Ratio of colocalization of RRβs between 9.8 and 18.2 or 29.2 mM glucose during staircase stimulation. **o**–**q**, Representative image of exocytosis (**o**), time-dependent fusion events (**p**) and two-round secretory capacity of β cells (**q**; $n = 416$) in repeat 18.2 mM glucose stimulation. R1, round 1; R2, round 2. **r**, Ratio of colocalization of RRβs and RIβs between two rounds of stimulations. Data are shown as mean ± s.e.m. in **b**–**d**, **g**–**j**, **l**–**n**, **p** and **r**. P values were calculated by a two-sided unpaired Student's t test. NS, not significant, $P > 0.05$; $^{*}P < 0.05$, $^{**}P < 0.01$, $^{***}P < 0.001$, $^{****}P < 0.0001$. Exact P values are provided in Supplementary Table 1. Datasets for single-step stimulation included three islets from two male mice, nine islets from five male mice, nine islets from three male and four female mice, or three islets from three male mice for 7, 9.8, 18.2 and 29.2 mM glucose, respectively; for staircase stimulation, we collected three islets from one male mouse. In **j** and **k**, RRβs consisted of 22 cells for 7 mM glucose, 98 cells for 9.8 mM glucose, 117 cells for 18.2 mM glucose and 40 cells for 29.2 mM glucose. In **p**–**r**, 11 islets were collected from four male and four female mice. Scale bar = 10 μm.

https://doi.org/10.1038/s42255-023-00962-0

27 ± 5 versus 4 ± 0.5 fusion events), the maximum amplitudes of the Ca^{2+} transients in RRβs were not different from those in RIβs (Fig. 3g). The only difference was the faster initiation speed in RRβs (Fig. 3h), which was partly due to a group of nonresponsive β cells exhibiting slower initiation speeds (Fig. 3i). Furthermore, we also analysed the relationship between RRβs and other specific cell types (for example, 'first-responder cells', 'hub cells') recently identified in terms of Ca^{2+} responses[16,17,29] (Extended Data Fig. 5). Consistent with the important

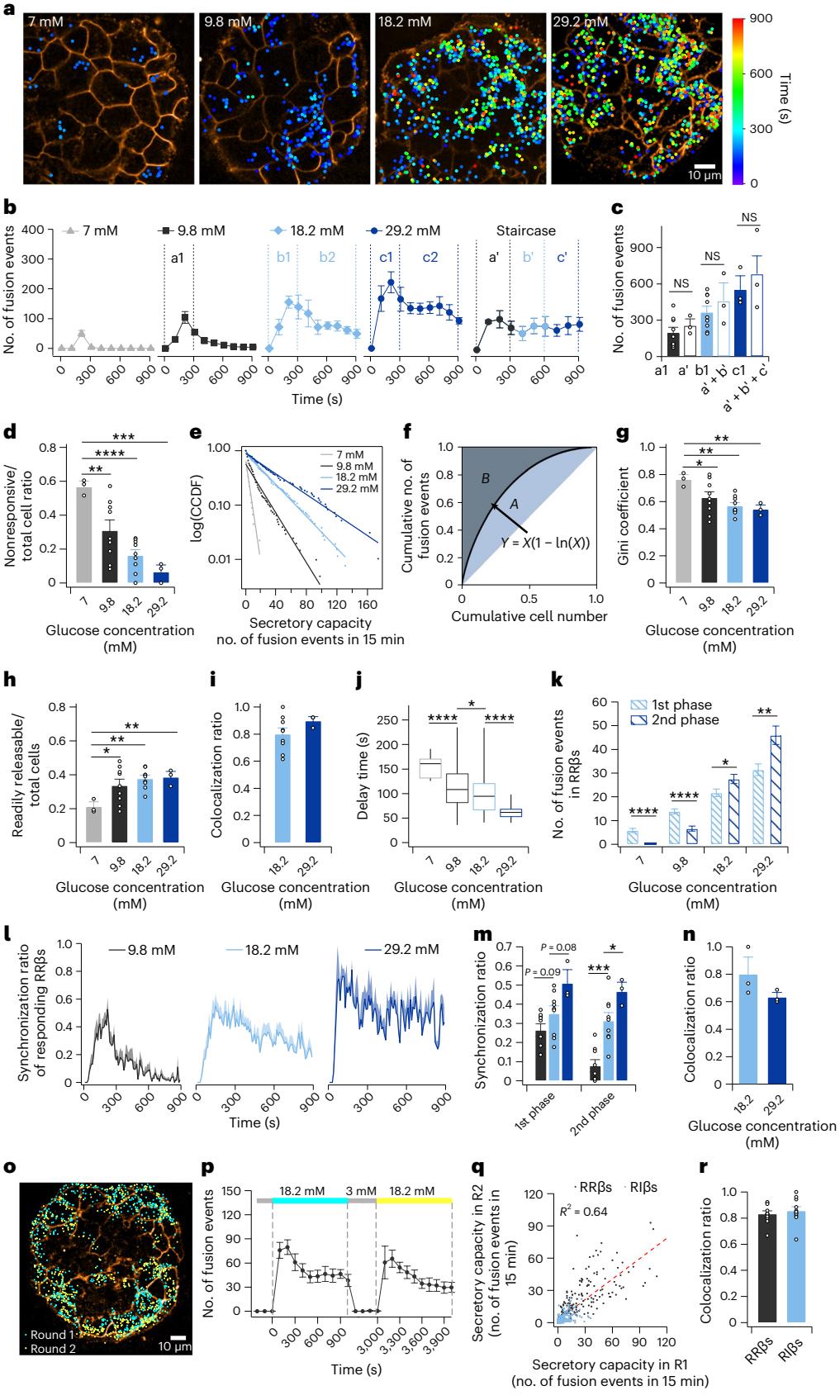

https://doi.org/10.1038/s42255-023-00962-0

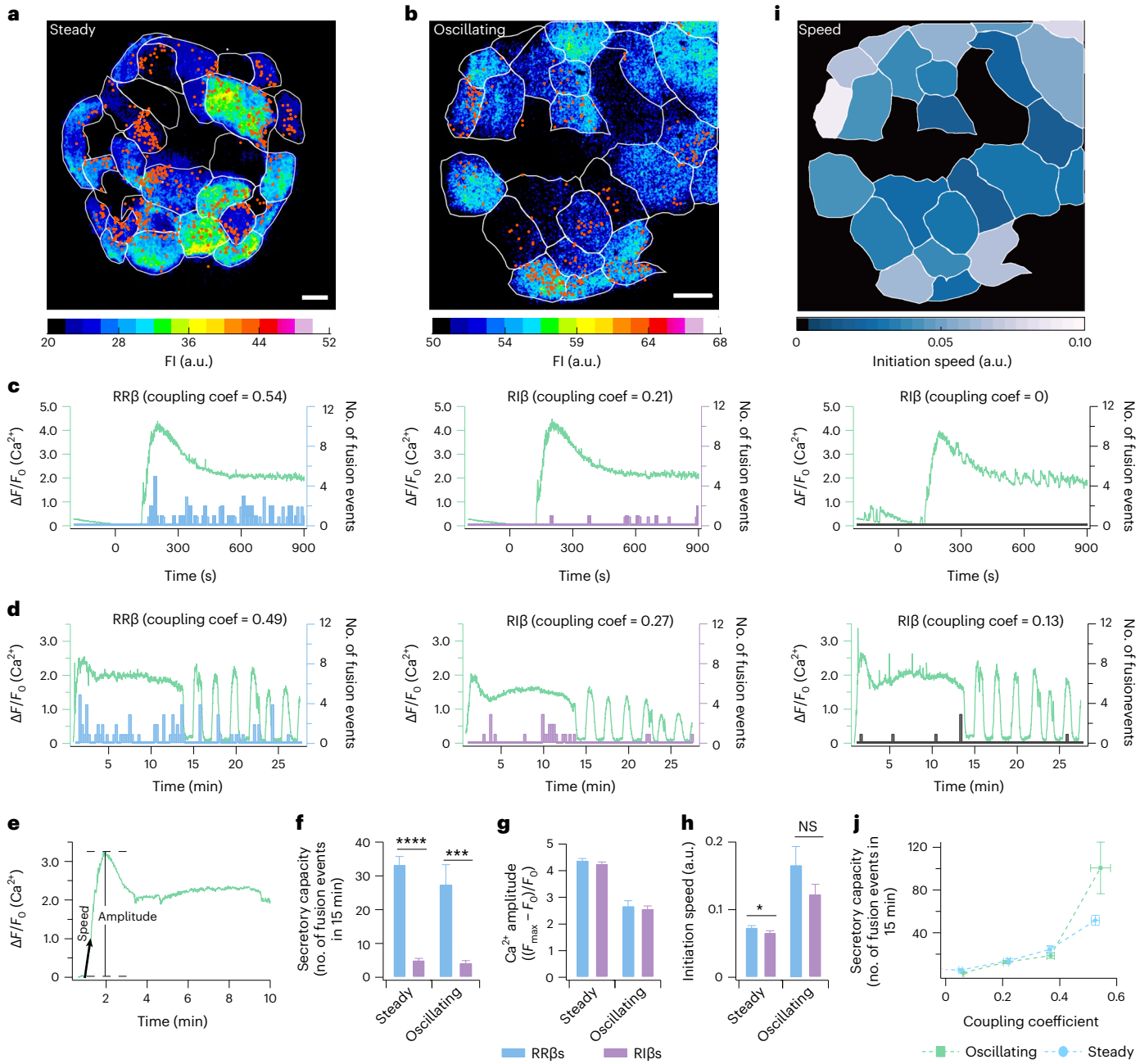

Fig. 3 | RRβs demonstrate tighter coupling between Ca^{2+} and secretion than RIβs. a,**b**, Representative examples of steady (**a**; from a female mouse) and oscillating (**b**; from a male mouse) Ca^{2+} signals (colour map) and fusion events (puncta) evoked by 18.2 mM glucose in an islet. The β cells are outlined by white circles. The colour map indicates the maximum-intensity *z* projection (arbitrary units (a.u.)) of the Ca^{2+} signal in each pixel during stimulation for 15 min (steady) or 28 min (oscillating). Fusion events are highlighted as red puncta. FI, fluorescence intensity. **c**,**d**, Coupling relationship between steady (**c**) or oscillating (**d**) Ca^{2+} signals (curve) and fusion events (histogram) in three individual β cells with different secretory capacities within the same islet. **e**, Example of Ca^{2+} transients evoked by 18.2 mM glucose in a β cell. Amplitude was defined as $(F_{max} - F_0)/F_0$. Initiation speed was defined as the initial slope of the Ca^{2+} influx (see details in Methods). **f**–**h**, Secretory capacity (**f**), maximum amplitude (**g**) and initiation speed (**h**) of Ca^{2+} transients in RRβs and RIβs under steady and oscillating Ca^{2+} dynamics. **i**, Colour-coded initiation speed (arbitrary units) of Ca^{2+} transients in individual β cells within the islet shown in **b**. **j**, The coupling coefficient between Ca^{2+} and secretion increased along with enhancement in the secretory capacity. Data are shown as mean ± s.e.m. in **f**–**h**. *P* values were calculated by a two-sided unpaired Student's *t* test. NS, $P > 0.05$; $^{*}P < 0.05$, $^{***}P < 0.001$, $^{****}P < 0.0001$. Exact *P* values are provided in Supplementary Table 1. For datasets in **f**–**h**: steady, $n = 79$ RRβs and 122 RIβs from six islets from one male and three female mice; oscillating, $n = 27$ RRβs and 38 RIβs from three islets from one male mouse. Data in **j**: $n = 201$ cells from six islets from one male and three female mice in steady Ca^{2+}; $n = 65$ cells from three islets from one male mouse in oscillating Ca^{2+}. Scale bar = 10 μm.

role of first-responder cells[29], 61–67% of these cells were classified as RRβs under both steady and oscillating Ca^{2+} dynamics. This percentage is notably higher than the percentage (17–33%) of 'second-follower cells' that overlapped with RRβs (Extended Data Fig. 5a). Under an oscillating second phase, 67% of leader cells[16] and 29% of hub cells[17] (defined by the top 10% of cells with the highest connection number) were RRβs. These results suggest that, with respect to Ca^{2+} dynamics, first-responder and leader cells exhibit a higher secretory capacity. In

contrast, second-follower and hub cells generally do not respond to glucose stimulation in terms of insulin secretion. However, heterogeneous Ca^{2+} signals within the islet are unlikely to be the primary force behind the variations observed in islet β cell secretion. Rather, we discovered that glucose-induced Ca^{2+} dynamics correlated well with secretions from RRβs, especially in an oscillating pattern. This sharply contrasted with the decoupled Ca^{2+} and secretion in RIβs (Fig. 3c,d,j; see Methods for coupling coefficients). Therefore, RIβs are deficient in Ca^{2+}–secretion coupling but not in glucose-stimulated Ca^{2+} signals per se.

SST modulates RRβs and the first phase of GSIS

SST released from islet δ cells inhibits the activities of neighbouring α and β cells[20,30,31] and thus might restrict islet β cells from secreting insulin. To test this hypothesis, we incubated islets with the SST type 2 receptor (SSTR2) antagonist CYN-154806 or exogenous SST before stimulation with glucose (18.2 mM) (Fig. 4a–c). Compared with the control, islets treated with 200 nM CYN-154806 showed a significantly potentiated first phase of GSIS: fusion events became more spatially homogeneous, accompanied by a reduction in the Gini coefficient (Fig. 4a,b,d,e). Correspondingly, the number of RRβs increased after CYN-154806 treatment, whereas their secretory abilities remained unaltered (Fig. 4f,g). Moreover, although CYN-154806 treatment did not increase RRβ synchronization, islet β cells responded more readily and synchronously to glucose stimulation (Fig. 4h,i), which also contributed to the pronounced first phase.

Conversely, the application of exogenous SST (100 nM) inhibited GSIS. A markedly diminished first phase of GSIS (Fig. 4c,j) resulted in fewer β cells being able to respond to glucose stimulation and in an increase in the Gini coefficient of the individual β cells (Fig. 4k,l). The average exocytosis of individual RRβs after SST treatment was not different from that of the control, despite a reduction in the first phase and an increase in the second phase (Fig. 4m). Similarly, SST delayed the first phase of GSIS and slightly reduced the synchronization among different cells (Fig. 4n,o). Thus, these loss-of-function and gain-of-function experiments reveal the indispensable role of SST in clamping β cells into RIβs.

We calculated the area occupied by each fusion event within a Voronoi diagram to evaluate the spatial heterogeneity of exocytosis (Fig. 5a,b and Methods). To compensate for the different fusion numbers, we constructed sub-Voronoi diagrams based on randomly truncated fusion events (400 events for CYN-154806 treatment and 150 events for SST treatment; Fig. 5c,d and Methods). CYN-154806 treatment eliminated the large patches; thus, the treated islets showed a homogeneous spatially distributed secretion (Fig. 5a,c,e,f). In contrast, SST treatment increased the large patches and made secretion more spatially heterogeneous (Figs. 5d and 5b,g,h). This was in contrast to the unaltered Gini coefficient in a reduced subset of randomly distributed fusion events compared with the complete set (Fig. 5i,j). By imaging insulin secretion in islets isolated from *Sst-Cre*$^{+}$; *tdTomato*$^{f/f}$ mice, in which δ cells were labelled with tdTomato (*Stdt* mice), we found an inverse relationship between the number of fusion events per islet and the number of δ cells within a ~15-μm volumetric scanning depth on the focus plane (Fig. 5k–m and Supplementary Video 3). To further investigate the effect of δ cells on RRβs or RIβs, we repeatedly stimulated an islet with glucose in the absence (first round) or presence (second round) of an SSTR antagonist. To our surprise, we did not observe a consistent enhancement of insulin secretion by adding MK-4256 (ref. 32), an SSTR3 antagonist, regardless of whether the islet was devoid of or enriched in δ cells. Instead, we noted an increase in glucose-stimulated secretion with CYN-154806 treatment in islets containing six to eight δ cells (Extended Data Fig. 6a–c). As SSTR2 is selectively expressed in mouse α cells[33], these results suggest that δ cells may indirectly inhibit β cell secretion by directly suppressing glucagon secretion from α cells. As glucagon enhances β cell secretion through both the glucagon receptor (GCGR) and glucagon-like peptide-1 receptor (GLP-1R)[34,35], we also investigated the effects of glucagon inhibition. When we synergistically applied MK 0893 and Exendin 9-39 (GCGR and GLP-1R antagonists) along with glucose, we observed a significant reduction in GSIS (Extended Data Fig. 6d,e). Therefore, the spatially heterogeneous β cell secretion may result from the combined inhibition and potentiation effects of neighbouring δ and α cells.

Aberrant insulin secretion of RRβs in *ob*/*ob* mice

Finally, we investigated biphasic GSIS in obese (*ob*/*ob*) mice of different ages. Compared with age-matched controls, *ob*/*ob* mice were notably more overweight and exhibited poorer glucose tolerance. As the mice aged, the discrepancies between *ob*/*ob* mice and the control group became increasingly pronounced (Extended Data Fig. 7). In islets from 4-week-old *ob*/*ob* mice, the ensemble biphasic GSIS was similar to that in islets from age-matched *Ins-GCaMP* mice; however, islets from adult *ob*/*ob* mice (>8 weeks) showed significantly diminished GSIS (Fig. 6a–d). Therefore, it became necessary to use a higher-affinity zinc dye (PKZnR-5 (ref. 28)) to detect fusion events. Nevertheless, the Gini coefficient of *ob*/*ob* islet cells was higher (0.68 in 4-week-old wild-type *ob*/*ob* islets versus 0.43 in *Ins-GCaMP* islets, 0.70 in adult *Ins-GCaMP ob*/*ob* (a hybrid mouse line generated by crossing *Ins-GCaMP* mice and *ob*/*ob* mice) islets versus 0.54 in *Ins-GCaMP ob*/wt islets; Fig. 6e), demonstrating more aggregating insulin secretion in space. Thus, compared with control islets, *ob*/*ob* islets comprised fewer RRβs (~26% of islet cells in 4-week-old mice and ~27% of islet cells in adult mice; Fig. 6f); however, their secretory capacity progressively decreased with age. In adolescent mice, these cells secreted more insulin granules, especially during the second phase; in adult mice, they released fewer insulin granules in both phases (Fig. 6g).

Interestingly, in both ages, these RRβs released insulin granules concurrently (Extended Data Fig. 8), which was defined as a 'burst' involving more than five or ten fusion events within a 10-s period in 4-week-old *ob*/*ob* or adult *Ins-GCaMP ob*/*ob* islets (as the number of fusion events in the first phase was 2.2-fold higher in adult *Ins-GCaMP ob*/wt islets than in 4-week-old *Ins-GCaMP* islets; Fig. 6h and Supplementary Video 4). In 4-week-old *ob*/*ob* islets, RRβs fired an average of ~1.5 bursts in 15 min, nearly three times more than that fired by RRβs from

Fig. 4 | SST clamps β cells and causes varied β cell secretions. a–**c**, Typical examples of islets treated with 18.2 mM glucose (control; **a**) or incubated with 200 nM CYN-154806 (CYN; **b**) or 100 nM SST (**c**). Colour-coded puncta represent fusion sites and time. **d**, Time-dependent fusion events in islets stimulated with 18.2 mM glucose (control, left) or incubated with CYN-154806 (right). **e**,**f**, Gini coefficient (**e**) and ratio of RRβs (**f**) under stimulation with 18.2 mM glucose (control) or incubation with CYN-154806. **g**, Exocytosis of RRβs in the first phase, second phase and both phases. **h**, Distribution of the delay time in RRβs. Centre line, median; limits, 75% and 25%; whiskers, maximum and minimum; solid circles, outliers. **i**, Synchronization of RRβs at 10-s intervals. **j**, Time-dependent fusion events in islets stimulated with 18.2 mM glucose (control, left) or incubated with SST (right). **k**,**l**, Gini coefficient (**k**) and ratio of RRβs (**l**) during stimulation with 18.2 mM glucose (control) or incubation with SST. **m**, Average exocytosis of RRβs in the first phase, second phase and both phases. **n**, Distribution of the delay time of RRβ secretion. Centre line, median; limits, 75% and 25%; whiskers, maximum and minimum; solid circles, outliers. **o**, Synchronization of RRβs at 10-s intervals. Data are shown as mean ± s.e.m. in **d**–**g**, **i**–**m** and **o**. Significance was evaluated by a two-sided unpaired Student's *t* test for mean (*). $^{*}P < 0.05$, $^{**}P < 0.01$, $^{***}P < 0.001$ and $^{****}P < 0.0001$. Exact *P* values are provided in Supplementary Table 1. In **h** and **n**, significance was also evaluated by an *F* test for s.d. (#). Datasets in control for CYN-154806 included three islets from two male mice; in CYN-154806, four islets from two male mice; in control for SST, three islets from two male mice; in SST, three islets from two male mice. In **g**, **h**, **m** and **n**, RRβs consisted of 39 (CYN-154806 control) or 44 (SST control) cells for control, 67 cells for CYN-154806, or 26 cells for SST. Scale bar = 10 μm.

https://doi.org/10.1038/s42255-023-00962-0

control *Ins-GCaMP* islets (Fig. 6i). The number of granules released during one burst was also higher from 4-week-old *ob*/*ob* RRβs (Fig. 6j), and these bursts occurred more frequently in the second phase (Fig. 6k). In contrast, in adult *Ins-GCaMP ob*/*ob* islets, RRβs fired an average of ~0.8 bursts in 15 min, which is only 1.6-fold of that fired by RRβs from littermate *ob*/wt islets (Fig. 6i). Moreover, the number of fusion events in bursts was not significantly different from that observed in *ob*/wt RRβs (Fig. 6j). Therefore, the holistic perspective of altered GSIS in

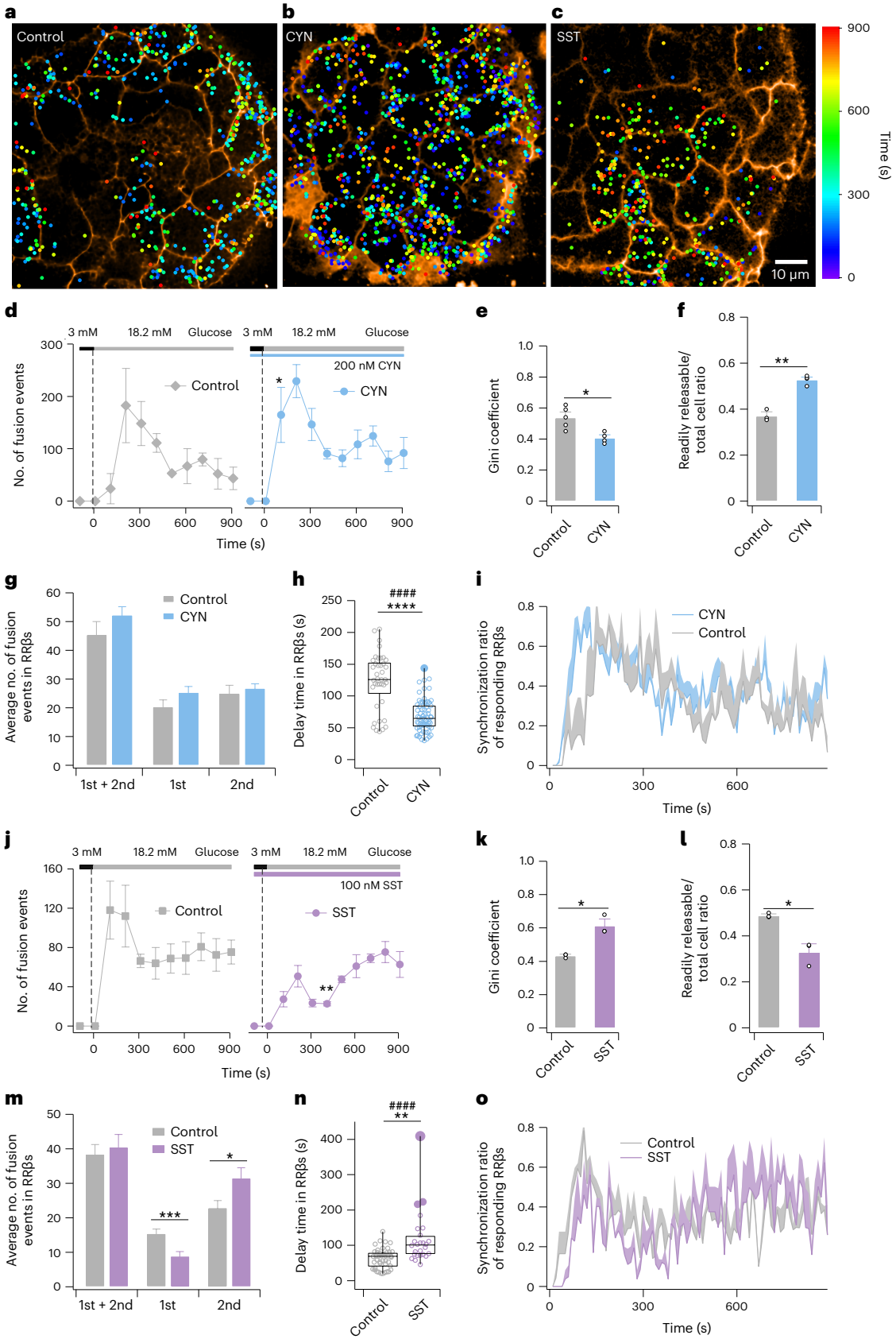

ob/*ob* mice includes decreased RRβ numbers, significantly increased secretion bursts and a progressively reduced secretion from individual RRβs with age.

To investigate the underlying mechanisms, we examined Ca^{2+} dynamics and secretion in adult *Ins-GCaMP ob*/*ob* islets compared with age-matched *Ins-GCaMP ob*/wt islets (Supplementary Videos 5 and 6). Consistent with previous data (Fig. 3), RRβs and RIβs demonstrated similar Ca^{2+} dynamics within the same islets, regardless of whether they were derived from control or *ob*/*ob* mice (Fig. 7a). As all β cells were labelled with GCaMP6f, we found that glucose stimulation failed to provoke any secretions from nearly 20% of β cells in adult *ob*/*ob* islets, a significantly higher proportion than that observed in their *ob*/wt counterparts (Fig. 7b,c). Furthermore, *Ins-GCaMP ob*/*ob* islets demonstrated low-amplitude but spiked Ca^{2+} dynamics (Fig. 7a,d,e), particularly a decreased amplitude of Ca^{2+} influx in the first phase, which may have contributed to the attenuated first phase of GSIS. The burst secretion was almost exclusively triggered by spiked Ca^{2+} transients (Fig. 7a). Although we have calculated burst secretions in *Ins-GCaMP* and adult *Ins-GCaMP ob*/wt islets in Fig. 6, they showed distinct Ca^{2+} transients (Fig. 7a). By using 50-s Ca^{2+} traces containing all fusion events for clustering by *t*-distributed stochastic neighbour embedding (*t*-SNE), we categorized Ca^{2+} dynamics associated with fusion events into three types: constant, increasing and spiked Ca^{2+} transients (Fig. 7f–h). In contrast to *Ins-GCaMP ob*/wt islets, nearly 74% of fusion events were triggered by spiked Ca^{2+} transients in *Ins-GCaMP ob*/*ob* islets (Fig. 7i); however, the secretory ability at high coupling coefficients was reduced in general (Fig. 7j). This suggests an adaptation by *ob*/*ob* islets to meet the increased insulin demand accompanying the decrease in the first phase. In summary, a reduced number of RRβs, a transition from constant to spiked Ca^{2+} dynamics, and a progressive diminishment in Ca^{2+} transients and insulin secretion from RRβs constitute the distinctive characteristics of GSIS in *ob*/*ob* islets.

Discussion

Regarding heterogeneous glucose-stimulated Ca^{2+} signals in islet β cells, the function of early-responder β cells has been intensely debated[36–38]. Some propose a disproportionate influence of these cells compared with other β cells within the islet[16,17], whereas others demonstrate that they are dispersible from glucose-evoked Ca^{2+} responses in islets[11,38]. However, we show that insulin secretion is critically controlled not by the heterogeneous Ca^{2+} kinetics in individual β cells per se but by the efficiency of stimulation–secretion coupling (Fig. 3). Additionally, despite a considerable overlap between 'leader cells' and 'first-responder cells' within RRβs, they represented only a small proportion of RRβs (Extended Data Fig. 5). The decoupling of Ca^{2+} and secretion in islet RIβs also underscores the necessity of directly detecting insulin secretion rather than indirectly evaluating β cell function using surrogates such as Ca^{2+} and redox states[11,16,17]. The glucose-refractory RIβs can be mobilized by relieving SST inhibition. SST released from δ cells is facilitated by urocortin 3 coreleased with insulin from β cells[39], and this corelease exhibits dynamic changes during disease progression in several diabetic mouse models[40]. Thus, δ cells and SST secretion may have a role in disease progression. In adult *ob*/*ob* mice, the notably diminished GSIS was attributed to both a decrease in the number of RRβs and their diminished secretory capacity (Fig. 6). The latter was due to the combination of reduced Ca^{2+} transients and changed patterns, as well as a decrease in the coupling (Fig. 7). As the local SST tone is reduced in type 2 diabetes[39,41], the significantly increased glucose-refractory behaviour of RIβs in *ob*/*ob* mice may be attributed to an autonomous failure of β cells. These data suggest that the heterogeneity in the secretory capacity of islet β cells may determine the GSIS status under both healthy and diseased conditions.

Although two-photon imaging has been used to visualize insulin secretion within islets[22,23], our method is more accurate and sensitive. In addition to specifically highlighting the exocytosis of zinc coreleased with insulin granules[42], we detected more than ~800 fusion events (using FluoZin-1) during 15 min of stimulation with an elevated glucose concentration (18.2 mM)—more than 16-fold higher than that detected using the two-photon method[22,23]. Only by visualizing many fusion events in islets can the ensemble evoked exocytosis recapitulate the kinetics measured by ELISA (Fig. 2b) and match the previously measured insulin secretion from the rat pancreas (compare Fig. 2b with Fig. 2 in ref. 25).

In addition to the reliable reconstruction of ensemble GSIS traces, our method permits assessing the contributions from individual β cells, which is beyond the detection of insulin secretion with ZIMIR (a cell surface-targeted zinc indicator for monitoring induced exocytotic release)[43]. Thus, we identified an exponential distribution of insulin secretion from β cells within the islet, and 40% of β cells activated by glucose contributed to most of the insulin secretion in the first and second phases of GSIS. The amplitude of the first phase of GSIS is determined mainly by RRβs in the islet, which are maximally mobilized and synchronized at glucose concentrations >18.2 mM. In contrast, the second phase of GSIS involves sustained exocytosis from RRβs, which might correspond to the continuous replenishment of the RRP vesicles postulated in the classical model[44]. In this regard, an even higher glucose concentration (29.2 mM) might replenish the vesicle pool more effectively, leading to more sustained exocytosis and better synchronization of individual RRβs and enhancing the second phase of GSIS (Fig. 2l,m).

Overall, using the novel imaging method developed in this study, we obtained an unexpected finding that RRβs within the islet, but not the RRP in all β cells, dictate the first phase of the biphasic GSIS. Specifically, increased secretion from individual RRβs accompanied by a reduced pool of RRβs was observed in islets from adolescent *ob*/*ob* mice, highlighting an early defect in the mobilization of RRβs during disease pathogenesis. With increased age, the secretion from RRβs is reduced and contributes to impaired GSIS. However, the present study has some limitations. For instance, most experiments were conducted at a glucose concentration of 18 mM, which represents a supraphysiological dose. Additionally, observations were made on isolated islets lacking microcirculation and innervation—conditions that may differ from those in vivo. Nevertheless, we believe that RRβ modulation could reveal new potential therapeutic targets for type 2 diabetes.

Fig. 5 | Pancreatic δ cells shape the spatially heterogeneous insulin secretion within islets. a,**b**, Example Voronoi diagrams under 18.2 mM glucose stimulation alone (control for CYN-154806 (CYN), 565 events; control for SST, 446 events) or incubation with CYN-154806 (745 events; **a**) or SST (195 events; **b**). The colour bar codes the percentage of occupied area (each islet area is normalized to 1). **c**,**d**, Sub-Voronoi diagram of 400 (**c**) and 150 (**d**) randomly sampled continuous fusion events within the islets shown in **a** and **b**, respectively. **e**–**h**, Plot of the occupied area of Voronoi patches (**e**, **g**) and sub-Voronoi patches (**f**, **h**) in a descending ranking. **i**,**j**, Frequency distribution of Gini coefficients under each random sampling (100 times for each islet) for control islets and islets treated with CYN-154806 (**i**) or SST (**j**). **k**, Representative images of islets containing either 1 δ cell (left; from a female mouse, islet 1 in Extended Data Fig. 6c) or 22 δ cells (right; from a female mouse, islet 6 in Extended Data Fig. 6c) within a volume of approximately 15-µm depth. Cyan dots represent fusion sites on the focus plane. **l**, Correlation of fusion events with the presence of δ cells within the islet volume. **m**, Overall count of fusion events in 15 min, observed under varying δ cell distributions. Data are shown as mean ± s.e.m. in **e**–**h** (error bands) and **m** (error bars). Significance was evaluated by a two-sided unpaired Student's *t* test for mean. $^{**}P < 0.01$. Exact *P* values are provided in Supplementary Table 1. For datasets in **a**–**j**, control for CYN-154806 included three islets from two male mice; control for SST, three islets from two male mice; CYN, four islets from two male mice; SST, three islets from two male mice. Data in **k**–**m** were collected from 14 islets from four male and three female mice; for each group in **m**, data were collected from 7 islets from five mice (>5 δ cells, two male and three female mice; <5 δ cells, three male and two female mice). Scale bar = 10 µm.

https://doi.org/10.1038/s42255-023-00962-0

Methods

Animals

C57BL/6N mice (aged 8–10 weeks) were purchased from Beijing Vital River Laboratory Animal Technology. Four- to 8-week-old *ob/ob* mice were purchased from GemPharmatech. Two- to 4-month-old *Stdt* mice[40] were a gift from X. Yu (Shandong University). *Ins-GCaMP* mice (aged 2–4 months) were cross-bred from the *Ins1-Cre*$^{+}$ (The Jackson Laboratory, stock no. 026801) and *GCaMP6f*$^{fl/f}$ (The Jackson Laboratory,

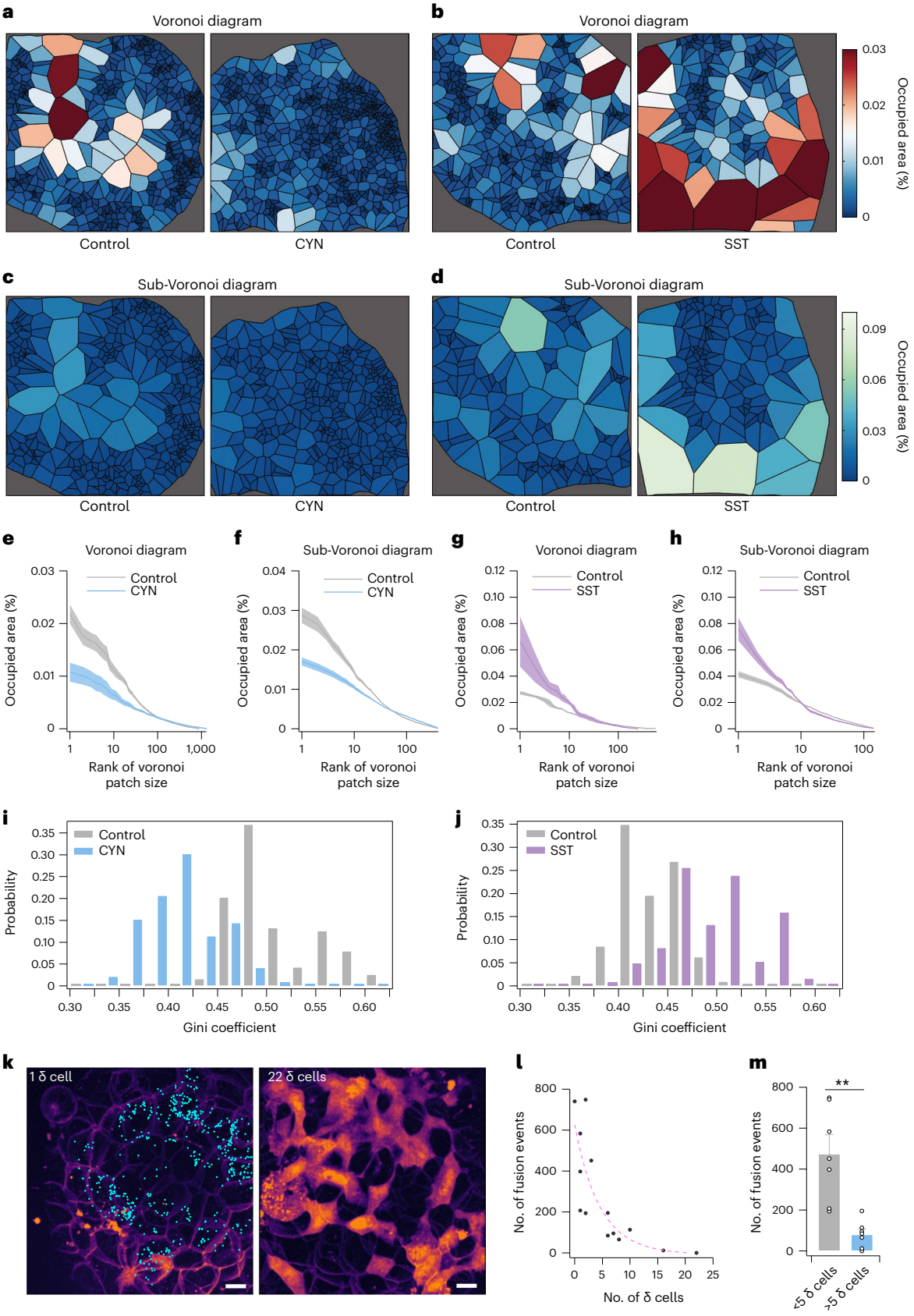

https://doi.org/10.1038/s42255-023-00962-0

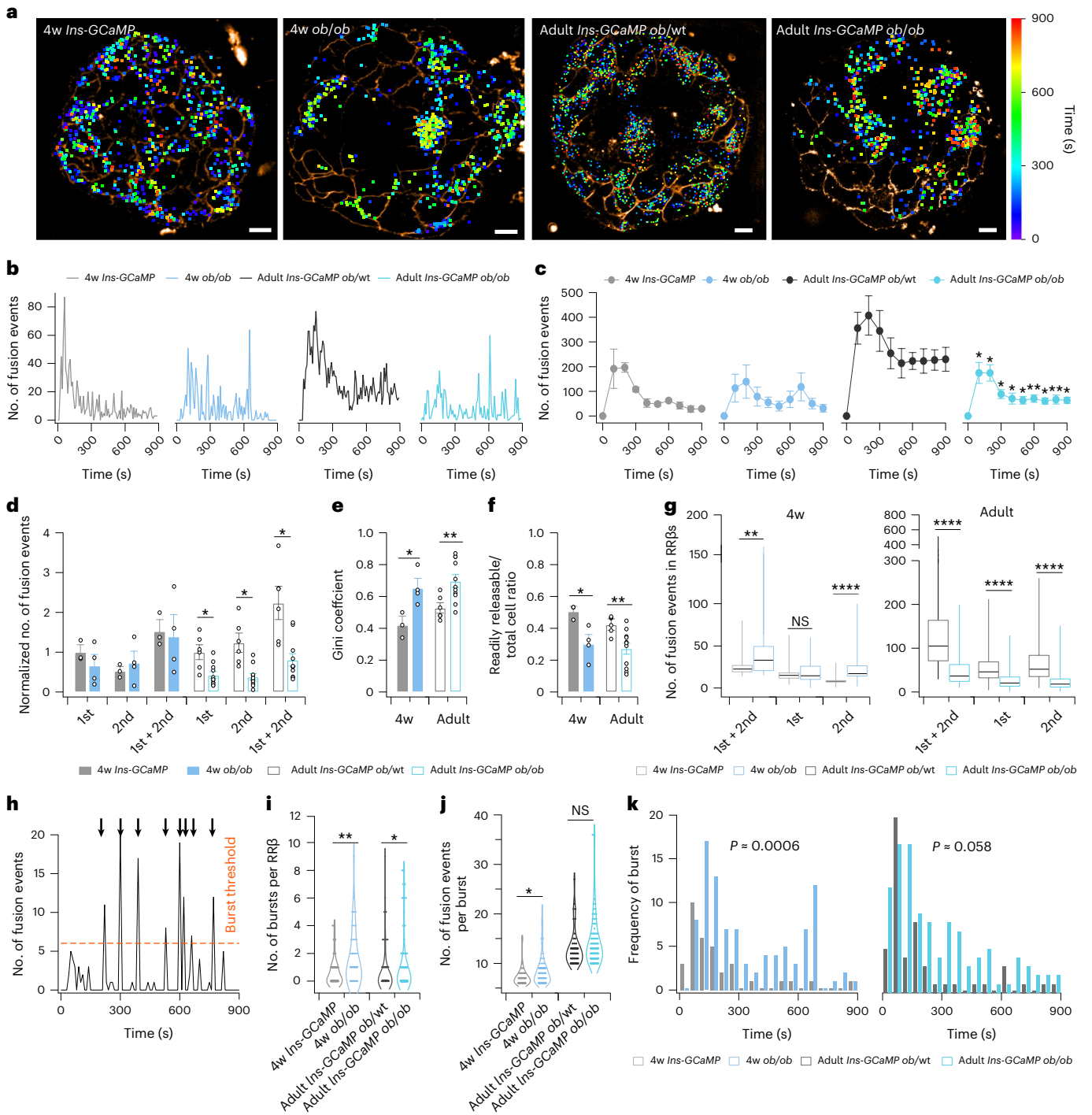

Fig. 6 | Aberrant insulin secretion of RRβs in *ob/ob* islets. a, Representative examples of secretion evoked by 18.2 mM glucose in 4-week-old (4w) *Ins-GCaMP* (male), 4-week-old *ob/ob* (male), and adult *Ins-GCaMP ob/ob* (female) mice and their littermates (*Ins-GCaMP ob*/wt, male). Colour-coded puncta represent fusion sites and time. **b**, Time-dependent histogram of fusion events in the islets shown in **a**. **c**, Time-dependent fusion events in 4-week-old and adult islets stimulated by 18.2 mM glucose. **d**, Statistics of fusion events in the first phase, second phase and both phases. **e**,**f**, Gini coefficient (**e**) and ratio of RRβs (**f**) in 4-week-old *Ins-GCaMP* and *ob/ob* islets and in adult *Ins-GCaMP ob*/wt and *Ins-GCaMP ob/ob* islets. **g**, Fusion events of RRβs in the first phase, second phase and both phases in 4-week-old *Ins-GCaMP* ($n = 60$ cells), 4-week-old *ob/ob* ($n = 53$ cells), adult *Ins-GCaMP ob*/wt ($n = 98$ cells) and adult *Ins-GCaMP ob/ob* ($n = 136$ cells) islets. Centre line, median; limits, 75% and 25%; whiskers, maximum and minimum. **h**, Definition of burst release (10-s period with more than five fusion events in 4-week-old islets or ten fusion events in adult islets), indicated by the arrows. **i**,**j**, Violin plots showing the number of bursts per RRβ (**i**) and fusion events per burst (**j**). Significance was evaluated by a Mann–Whitney *U* test. **k**, Histogram distribution of the occurrence time of bursts. Significance was evaluated by a Kolmogorov–Smirnov test. Data are shown as mean ± s.e.m. in **c**–**f**. Significance was evaluated by a two-sided unpaired Student's *t* test for mean. $^{*}P < 0.05$, $^{**}P < 0.01$, $^{****}P < 0.0001$. Exact *P* values are provided in Supplementary Table 1. For datasets in **c**–**k**: 4-week-old *Ins-GCaMP*, $n = 3$ islets from two male mice; 4-week-old *ob/ob*, $n = 4$ islets from two male mice; adult *Ins-GCaMP ob*/wt, $n = 6$ islets from three male mice and one female mouse; *Ins-GCaMP ob/ob*, $n = 11$ islets from two male and two female mice. For datasets in **i**–**k**: 34 bursts from 60 cells from 4-week-old *Ins-GCaMP* mice, 79 bursts from 53 cells from *ob/ob* mice, 51 bursts from 98 cells from *Ins-GCaMP ob*/wt mice and 110 bursts from 136 cells from *Ins-GCaMP ob/ob* mice. Scale bar = 10 µm.

https://doi.org/10.1038/s42255-023-00962-0

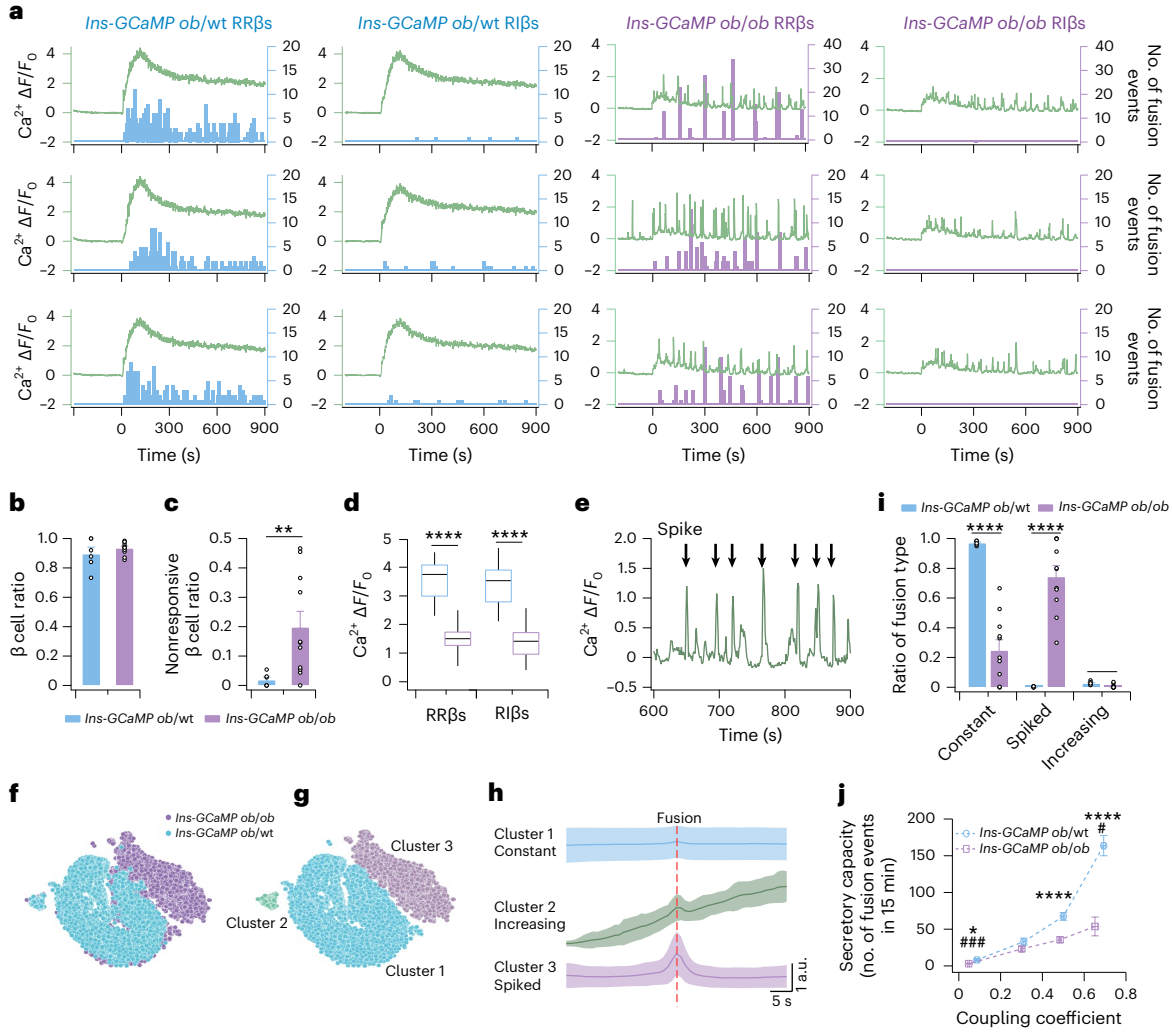

Fig. 7 | Spiked Ca^{2+} transients triggered burst secretion in *ob/ob* islets. **a**, Three examples of Ca^{2+} signals (curve) and fusion events (histogram) in RRβs and RIβs within the same *Ins-GCaMP ob*/wt islet (from a male mouse) or *Ins-GCaMP ob/ob* islet (from a female mouse) stimulated with 18.2 mM glucose. **b**,**c**, Proportion of β cells (**b**) and ratio of nonresponsive β cells to all β cells (**c**) in *Ins-GCaMP ob*/wt and *Ins-GCaMP ob/ob* islets. **d**, Maximum amplitude of Ca^{2+} influx in the first phase in RRβs and RIβs. $n = 98$ RRβs and 109 RIβs from 6 *Ins-GCaMP ob*/wt islets; $n = 135$ RRβs and 334 RIβs from 11 *Ins-GCaMP ob/ob* islets. **e**, Example of spiked Ca^{2+} signals in *ob/ob* islets. **f**,**g**, t-SNE plot visualized fusion events in *Ins-GCaMP ob*/wt ($n = 15{,}823$ fusion events) and *Ins-GCaMP ob/ob* ($n = 9{,}588$ fusion events) islets (**f**), and grouped fusion events into three clusters (**g**). **h**, Average Ca^{2+} signals of three types of fusion events. **i**, Ratio of three types of fusion events in *Ins-GCaMP ob*/wt and *Ins-GCaMP ob/ob* islets. **j**, Coupling coefficient of β cells in *Ins-GCaMP ob*/wt ($n = 228$ cells) and *Ins-GCaMP ob/ob* ($n = 482$ cells) islets. # and * represent the significance of the coupling coefficient and secretory capacity, respectively. Data are presented as mean ± s.e.m. (**c**, **d**, **i**, **j**) or mean ± s.d. (**h**). Significance was evaluated by a two-sided unpaired Student's *t* test for mean (*). $^{*}P < 0.05$, $^{**}P < 0.01$, $^{***}P < 0.001$, $^{****}P < 0.0001$. Exact *P* values are provided in Supplementary Table 1. For all datasets: adult *Ins-GCaMP ob*/wt, $n = 6$ islets from three male mice and one female mouse; adult *Ins-GCaMP ob/ob* islets, $n = 11$ islets from two male and two female mice.

stock no. 029626) lines. *Ins-GCaMP ob/ob* mice were cross-bred from *Ins-GCaMP* mice and *ob/ob* mice, and their littermates (*Ins-GCaMP ob*/wt) were used as controls. Two- to 3-month-old *Glu-GCaMP* mice were cross-bred from the *Glu-Cre* (kindly gifted by H.Y. Gaisano from the University of Toronto, Canada) and *GCaMP6f* lines. The mice were genotyped by PCR using template tail DNA, extracted with 50 mM NaOH (for *Stdt* mice) or the TIANamp Genomic DNA Kit (TIANGEN, DP304-03, for *Ins-GCaMP* mice). *Stdt* mice were genotyped with primers (mutant forward 5′-GGTACATGGATCCACTAGTTCT-3′, wild-type forward 5′-GAGGTCTGCCAACTCGAAC, common reverse 5′-AGTCAAACGCTTGCTCTT CA-3′) for SST-driven *Cre* recombinase and primers (forward 5′-CACTTGCTCTCCCAAAGTCG, wild-type reverse 5′-TAGTCTAACTCGCGACACTG-3′, mutant reverse 5′-GTTATGTAACGCGGAACTCC-3′) for *tdTomato*. The primers and protocols for genotyping *Ins-GCaMP* mice are available online. All mice were genotyped by PCR using 2× EasyTaq PCR SuperMix (TransGen). The animals were maintained in a specific pathogen-free animal facility at Peking University, housed in a 12-h light/12-h dark cycle with 22 °C temperature and 40–60% humidity, and administered water and chow diet ad libitum. The experiments were approved by the Ethics Committee of Peking University and performed at the animal facility of Peking University, which was accredited by the Association for Assessment and Accreditation of Laboratory Animal Care International.

Isolation and culture of mouse islets

Mice were killed by cervical dislocation, and primary islets were isolated as previously described[24]. The islets were maintained in RPMI 1640 medium (Gibco, 11879-020) containing 8 mM glucose, 10% FBS and 100 U penicillin–streptomycin overnight at 37 °C in an incubator with 5% CO_2.

Glucose tolerance test in *ob*/*ob* mice

For the glucose tolerance test, *ob*/*ob* mice were fasted for 6 h and then administered 1 g kg^{-1} glucose (Sigma, G7021) by intraperitoneal injection. Blood was sampled through a tail nick, and blood glucose level was measured using a blood glucose metre (Roche, Accu-Chek Active) at 0, 15, 30, 60, 90 and 120 min after glucose administration.

Fluorescence imaging of islets

All procedures were performed at 35–37 °C. The islets were seeded on a 35-mm glass-bottom confocal dish (Cellvis, D35-14-1-N) for >24 h to facilitate their adhesion. Before imaging, the islets were washed twice and bathed in KRBB solution containing 125 mM NaCl, 5.9 mM KCl, 2.4 mM $CaCl_2$, 1.2 mM $MgCl_2$, 1 mM L-glutamine, 25 mM HEPES, 3 mM glucose, 0.1% BSA and 8 μM Zn dye (FluoZin-1, Thermo Fisher Scientific, F24180; PKZnR-1 and PKZnR-5, synthesized by our laboratory[28]) for 15–30 min until resting. In experiments using CYN-154806 (Tocris, 1843), SST (Tocris, 1157) and MK 0893 (MedChemExpress, HY-50663) + Exendin 9-39 (Sigma, E7269), the islets were incubated in 3 mM glucose–KRBB solution containing either 200 nM CYN-154806, 100 nM SST or 1 μM MK 0893 + 1 μM Exendin 9-39 for 15–30 min. After resting the islets, images were acquired with a spinning-disc confocal microscope based on a CSU-X1 Yokogawa head mounted on an inverted IX81 Olympus microscope equipped with a ×100 (NA1.30, Olympus) or ×60 (NA1.35, Olympus) oil immersion objective lens. Images were captured either by an electron-multiplying charge-coupled device camera (Andor iXon3 897) or a scientific complementary metal–oxide semiconductor camera (C14440-20UP, Hamamatsu, Japan). All devices were controlled by MetaMorph software (Molecular Devices). We usually obtained recordings at 2–5 min before stimulation and 15 or 30 min after glucose stimulation. At the end of the stimulation, we labelled the islet plasma membrane using 10 μM FM 4-64 (Thermo Fisher Scientific, T3166). Notably, for *Stdt* mice, we usually began by imaging δ cells and then observing secretion using Zn^{2+} dye. Subsequently, we labelled the islet membrane with FM 4-64 and captured images of the cell boundaries.

For the repeat stimulation by perfusion in Fig. 2 and Extended Data Figs. 4 and 6, the pretreatment process was similar to the above procedure. However, after resting, islets were transferred to the perfusion system (Extended Data Fig. 4a), and then the solution was changed using a syringe and syringe pump (Harvard Apparatus). After preincubating the islets in 3 mM glucose–KRBB solution for 15 min, we recorded the basal images and then stimulated the islets with 18.2 mM glucose–KRBB for 15 min. After the first round of stimulation, the medium was reverted to 3 mM glucose–KRBB solution for 30 min to reset the islets (no image recording), and then the islets were restimulated with 18.2 mM glucose–KRBB solution. Finally, we added 10 μM FM 4-64 to label the plasma membrane.

Semi-automatic identification and analysis of fusion events

Because we applied the membrane-impermeable Zn^{2+} dye outside the cells, fluorescent puncta (zinc flickers) only emerged after the insulin vesicles had collapsed into the plasma membrane. Therefore, we used customized software to detect increases and decreases in fluorescence intensities associated with discrete fusion events[45]. Specifically, we selected events with increases in fluorescence intensity (F_1) greater than the background fluorescence (F_0) by a certain ratio ($R_1 > 1.1$) as possible fusion events. In addition, we used consecutive image subtraction to normalize the background fluorescence intensity across the entire field of view. We detected possible fusion events as a local increase in the fluorescence intensity over a preset ratio ($R_2 > 2.2$). Based on these criteria, we were able to detect most fusion events, which were manually confirmed later. Finally, we used two-dimensional Gaussian fitting and spatiotemporal analysis to extract additional information. The parameters mainly included the time points (appearance (T_1), brightest intensity (T_2) and disappearance (T_3)) and spatial location (x, y) of fusion events.

Alternatively, when fusion events were detected using PKZnR-5, images were denoised using the deep learning-based differential DeepCAD-RT algorithm (modified from DeepCAD-RT[46]) to adapt for temporal leakage and signal loss. Initially, we used the original images of fusion to train a customized DeepCAD-RT denoising model. Subsequently, we transformed each frame of raw data into three frames by calculating the difference between the current and previous frames, the difference between the current frame and the spatial–temporal averaging of the raw data, and the difference between the current and subsequent frames. By inputting the processed vesicle secretion data into the trained DeepCAD-RT model, we effectively reduced noise and obtained the denoised result by subtracting the middle frame of the three frames accordingly. As fused vesicles exhibit a point-like shape, we leveraged the power of TrackMate's LoG (Laplacian of Gaussian) operator to perform accurate puncta recognition on a frame-by-frame basis. After successful recognition, we used the simple linear assignment problem tracker in TrackMate to address the inherent characteristics of vesicles, namely running on the membrane surface and the occasional presence of gap-closing events due to defocusing. To address these considerations, we allowed for a seamless connection of the identified vesicles across frames and the creation of traceable trajectories. Finally, we selected single spots and trajectories as possible fusion events and checked all possible fusion events individually to confirm the true fusion events.

GSIS measured by ELISA

To obtain the data shown in Extended Data Fig. 1c, 20 islets for each group from the same mouse were preincubated in 2 ml of KRBB solution containing 3 mM glucose for 30 min at 37°C until resting and then transferred to another 200 μl of KRBB solution containing 3 mM glucose for 5 min. The corresponding solution was collected at the 0-min time point. The islets were transferred into 200 μl of KRBB solution containing 20 mM glucose for glucose stimulation, and 50 μl of the solution was withdrawn at 2, 5, 10, 20 and 30 min for the quantification of insulin. Insulin quantification was performed using a rat/mouse insulin ELISA kit (Millipore, EZRMI-13K) following the manufacturer's instructions.

CCDF and exponential distribution

We used the CCDF to depict the heterogeneity of the secretory capacity of responsive cells. In this analysis, the secretory capacity of a single cell during a 15-min stimulation period was defined as s. The number of cells with a secretory capacity of s was denoted as $n(s)$. The total number of responsive cells from all islets was denoted as N. The total number of fusion events across all islets was denoted as S. The number of cells with a secretory capacity higher than s was represented as $N(s)$. Then

$$N(s) = \int_s^{+\infty} n(s)\mathrm{d}s, \tag{1}$$

and the CCDF was calculated as $N(s)/N$ (Extended Data Fig. 2c).

When the CCDF was plotted on a semilogarithmic graph (Fig. 2e), it aligned well with a straight line. This suggests that the CCDF adhered closely to an exponential function:

$$\frac{N(s)}{N} = \mathrm{e}^{-ks}. \tag{2}$$

The value of the parameter k varied depending on the glucose concentration.

By taking the derivative, the probability density function is

$$\frac{n(s)}{N} = k \times \mathrm{e}^{-ks}. \tag{3}$$

Gini coefficient

To calculate the Gini coefficient, we first computed the Lorenz curve (showing the relationship between the cumulative ratio of participating cells and the cumulative secretion ratio). Specifically, the cumulative

ratio of participating cells, X, and the cumulative secretion ratio, Y, were defined as

$$X = X(s) = \frac{\int_s^{+\infty} n(s)\mathrm{d}s}{\int_0^{+\infty} n(s)\mathrm{d}s} = \frac{\int_s^{+\infty} n(s)\mathrm{d}s}{N} = \frac{N(s)}{N} \tag{4}$$

and

$$Y = Y(s) = \frac{\int_s^{+\infty} s \times n(s)\mathrm{d}s}{\int_0^{+\infty} s \times n(s)\mathrm{d}s} = \frac{\int_s^{+\infty} s \times n(s)\mathrm{d}s}{S}. \tag{5}$$

In a homogeneous system, X is proportional to Y (that is, $Y = X$). However, in an exponential system, X and Y follow the relationship $Y = (1 - \ln(X))X$. The proof is shown below.

Starting from equation (5), we have

$$\int_s^{+\infty} s \times n(s)\mathrm{d}s = Y \times \int_0^{+\infty} s \times n(s)\mathrm{d}s. \tag{6}$$

Combining equation (6) with equation (2), we get

$$\int_s^{+\infty} s \times N \times k \times \mathrm{e}^{-ks}\mathrm{d}s = Y \times \int_0^{+\infty} s \times N \times k \times \mathrm{e}^{-ks}\mathrm{d}s. \tag{7}$$

The left side of equation (7) can be simplified as follows:

$$\begin{aligned}\int_s^{+\infty} s \times N \times k \times \mathrm{e}^{-ks}\mathrm{d}s &= -N \times \int_s^{+\infty} s\mathrm{d}\mathrm{e}^{-ks} \\ &= -N\left(s \times \mathrm{e}^{-ks}\big|_s^{+\infty} - \int_s^{+\infty} \mathrm{e}^{-ks}\mathrm{d}s\right) \\ &= -N \times \left(s \times \mathrm{e}^{-ks}\big|_s^{+\infty} + \frac{1}{k} \times \mathrm{e}^{-ks}\big|_s^{+\infty}\right) \\ &= N \times \left(x + \frac{1}{k}\right) \times \mathrm{e}^{-ks}.\end{aligned} \tag{8}$$

Thus, from equations (7) and (8), we obtain

$$\begin{aligned}N \times \left(s + \frac{1}{k}\right) \times \mathrm{e}^{-ks} &= Y \times N \times \left(0 + \frac{1}{k}\right) \times \mathrm{e}^{-k\times 0} \\ (ks + 1) \times \mathrm{e}^{-ks} &= Y\end{aligned}. \tag{9}$$

From equations (2) and (4), we can express X as

$$X = \mathrm{e}^{-ks}. \tag{10}$$

Now, combining equations (9) and (10), we get

$$(1 - \ln(X))X = Y. \tag{11}$$

This shows that X nonlinearly contributes to Y. For example, 40% of the cells contribute approximately 80% of the total release; that is

$$(1 - \ln(0.4))\,0.4 = 0.76. \tag{12}$$

As shown in Fig. 2f, the Gini coefficient is defined as the ratio of the area of A (the area that lies between the line of equality and the Lorenz curve) to the area of A and B (the total area above the line of equality), which is

$$\begin{aligned}\mathrm{Gini} &= \frac{A}{A+B} \\ \mathrm{Gini} &= \frac{\int_0^1 Y(X) - X\mathrm{d}X}{\int_0^1 X\mathrm{d}X} = \frac{\int_0^1 Y(X)\mathrm{d}X - 0.5}{0.5}\end{aligned}. \tag{13}$$

According to this equation, the Gini coefficient of the exponential distribution is a constant 0.5, independent of the parameter k. The proof is shown below.

Starting from equations (11) and (13), we have

$$\begin{aligned}\int_0^1 Y(X)\,\mathrm{d}X &= \int_0^1 x(1 - \ln(x))\,\mathrm{d}x = 0.5\int_0^1 (1 - \ln(x))\,\mathrm{d}x^2 \\ &= 0.5\left((1 - \ln(x))x^2\big|_0^1 - \int_0^1 x^2\mathrm{d}(1 - \ln(x))\right) \\ &= 0.5\left((1 - \ln(x))x^2\big|_0^1 + \int_0^1 x\mathrm{d}x\right) \\ &= 0.5\left((1 - \ln(x))x^2\big|_0^1 + 0.5x^2\big|_0^1\right) \\ &= 0.75.\end{aligned} \tag{14}$$

From equations (13) and (14), we obtain

$$\mathrm{Gini} = 0.5. \tag{15}$$

While determining the experimental Gini coefficient of each islet, we ordered the secretory capacity of all cells within a single islet, encompassing both responsive and nonresponsive cells, in a descending sequence: $s_1 > s_2 > s_3 \ldots > s_n$. The total cell number of one islet was defined as N_{islet}, and the total number of fusion events was defined as S_{islet}.

Then, we calculated the cumulative ratio of participating cells, $X(n)$:

$$X(n) = \frac{n}{N_{\mathrm{islet}}}, \tag{16}$$

and the cumulative ratio of fusion events, $Y(n)$:

$$Y(n) = \frac{\sum_{i=1}^{n} s_i}{S_{\mathrm{islet}}}. \tag{17}$$

Finally, according to equation (13), we calculated the experimental Gini coefficient of each islet.

Synchronization and delay time in RRβs

The synchronization ratio was calculated as the ratio of responsive RRβs to the total number of RRβs at a given time (10-s intervals). The delay time was defined as the time gap between the increase in glucose concentration and the emergence of the first fusion event in each RRβ.

Ca^{2+} amplitude, initiation speed, and coupling between secretion and Ca^{2+} signals

The basal Ca^{2+} fluorescence intensity before Ca^{2+} influx in each cell was denoted as F_0 (the corresponding time was t_0), and the maximal Ca^{2+} fluorescence intensity reached during the first phase was denoted as F_{max}. Time t_0 plus 20 frames was defined as t_{20}, and the corresponding fluorescence intensity was defined as F_{20}. The initiation speed was defined as $(F_{20} - F_0)/(t_{20} - t_0)$. The Ca^{2+} amplitude was defined as $(F_{max} - F_0)/F_0$.

For the coupling coefficient, the intensity of Ca^{2+} signals was denoted as $\mathrm{Ca}(t)$. Fusion events were discretized into 20 s per bin. The number of fusion events was denoted as $Q(t)$, and then the bins were linearly interpolated to the same dimension as $\mathrm{Ca}(t)$. The Pearson linear correlation coefficient between $Ca(t)$ and $Q(t)$ was defined as the coupling coefficient between the Ca^{2+} signal and the secretion.

In Fig. 7d, for all Ca^{2+} traces of *Ins-GCaMP ob/ob* islet cells, we used the movmin function in MATLAB to extract the basic Ca^{2+} dynamics and then identified the maximum value as the maximum amplitude of the Ca^{2+} signal.

t-SNE clustering of fusion events

In Fig. 7, we extracted a total of 50 s of Ca^{2+} traces, encompassing 25 s before and 25 s after each fusion event, within adult *Ins-GCaMP ob*/wt and *ob/ob* islets. Following this, we used the *t*-SNE technique to categorize these fusion-related Ca^{2+} traces. This resulted in the traces being grouped into three distinct clusters.

Two-dimensional spatial heterogeneity analysis using Voronoi diagrams

We used a Voronoi diagram (MATLAB Voronoi function) segmenting the occupied area of each fusion event to evaluate the two-dimensional spatial heterogeneity of vesicle fusion. Each fusion site was the centre point of one Voronoi patch (Fig. 5a,b). Therefore, large or small Voronoi patches indicated regions with few or many fusion events. The total islet area was normalized to 1. As the total number of fusion events changed under different conditions, we used sub-Voronoi diagrams to correct the differences in exocytosis (Fig. 5c,d). Specifically, we randomly selected 400 continuous fusion events from control islets or islets treated with CYN-154806 or 150 fusion events from control islets or islets incubated with SST. We next performed five rounds of random sampling for each islet. Then, we combined all occupied areas to create a descending ranking (Fig. 5f,h). Results obtained with selections of sub-Voronoi diagrams were similar to those obtained with the complete set of Voronoi analyses. Finally, to evaluate whether random sampling alters cellular heterogeneity, we also calculated the Gini coefficient under each random sampling (100 times for each islet; Fig. 5i,j) and confirmed that random sampling did not alter the overall characteristics of the original data.

Statistics and reproducibility

Igor Pro 8.0 (WaveMetrics) was used to prepare the figures and conduct statistical analyses. Results are presented as mean ± s.e.m. unless otherwise indicated in the figure legend. Each independent experiment was performed with at least three biological replicates, and sample sizes were determined according to those used in similar studies. Statistical significance for two-group comparisons was tested using either Student's *t* test for single Gaussian-distributed datasets or the Mann–Whitney *U* test for nonsingle Gaussian-distributed datasets. Statistical significance was defined as $P < 0.05$. Exact *P* values and other detailed statistical information for each figure are provided in Supplementary Table 1. *, **, *** and **** were used to represent *P* values less than 0.05, 0.01, 0.001 and 0.0001, respectively.

Reporting summary

Further information on research design is available in the Nature Portfolio Reporting Summary linked to this article.

Data availability

Data supporting the findings of this study are available in the figures and extended data figures. Other related data are available from the authors on reasonable request. As the original images contain other information that needs to be analysed, we cannot upload all of them to a publicly accessible repository presently. Instead, typical videos showing our signals are provided as supplementary data. However, if anyone is interested in them, original images may be requested from the corresponding authors. Source data are provided with this paper.

Code availability

Custom code and algorithm are available in Methods, publications from our laboratory (cited in the main text) or from the authors on request.

References

1. Cerasi, E. & Luft, R. The plasma insulin response to glucose infusion in healthy subjects and in diabetes mellitus. *Acta Endocrinol. (Copenh.)* **55**, 278–304 (1967).
2. Simpson, R. G., Benedetti, A., Grodsky, G. M., Karam, J. H. & Forsham, P. H. Early phase of insulin release. *Diabetes* **17**, 684–692 (1968).
3. Martinussen, C. et al. Immediate enhancement of first-phase insulin secretion and unchanged glucose effectiveness in patients with type 2 diabetes after Roux-en-Y gastric bypass. *Am. J. Physiol. Endocrinol. Metab.* **308**, E535–E544 (2015).
4. Barg, S., Eliasson, L., Renstrom, E. & Rorsman, P. A subset of 50 secretory granules in close contact with L-type Ca^{2+} channels accounts for first-phase insulin secretion in mouse β-cells. *Diabetes* **51**, S74–S82 (2002).
5. Schulla, V. et al. Impaired insulin secretion and glucose tolerance in β cell-selective $Ca_V1.2$ Ca^{2+} channel null mice. *EMBO J.* **22**, 3844–3854 (2003).
6. Jing, X. et al. $Ca_V2.3$ calcium channels control second-phase insulin release. *J. Clin. Invest.* **115**, 146–154 (2005).
7. Kang, L. et al. Munc13-1 is required for the sustained release of insulin from pancreatic β cells. *Cell Metab.* **3**, 463–468 (2006).
8. Pipeleers, D., Kiekens, R., Ling, Z., Wilikens, A. & Schuit, F. Physiologic relevance of heterogeneity in the pancreatic beta-cell population. *Diabetologia* **37**, S57–S64 (1994).
9. Pipeleers, D. G. Heterogeneity in pancreatic β-cell population. *Diabetes* **41**, 777–781 (1992).
10. Benninger, R. K. P. & Hodson, D. J. New understanding of β-cell heterogeneity and in situ islet function. *Diabetes* **67**, 537–547 (2018).
11. Westacott, M. J., Ludin, N. W. F. & Benninger, R. K. P. Spatially organized β-cell subpopulations control electrical dynamics across islets of Langerhans. *Biophys. J.* **113**, 1093–1108 (2017).
12. Dorrell, C. et al. Human islets contain four distinct subtypes of β cells. *Nat. Commun.* **7**, 11756 (2016).
13. Segerstolpe, A. et al. Single-cell transcriptome profiling of human pancreatic islets in health and type 2 diabetes. *Cell Metab.* **24**, 593–607 (2016).
14. Jetton, T. L. & Magnuson, M. A. Heterogeneous expression of glucokinase among pancreatic beta cells. *Proc. Natl Acad. Sci. USA* **89**, 2619–2623 (1992).
15. Piston, D. W., Knobel, S. M., Postic, C., Shelton, K. D. & Magnuson, M. A. Adenovirus-mediated knockout of a conditional glucokinase gene in isolated pancreatic islets reveals an essential role for proximal metabolic coupling events in glucose-stimulated insulin secretion. *J. Biol. Chem.* **274**, 1000–1004 (1999).
16. Salem, V. et al. Leader β-cells coordinate Ca^{2+} dynamics across pancreatic islets in vivo. *Nat. Metab.* **1**, 615–629 (2019).
17. Johnston, N. R. et al. Beta cell hubs dictate pancreatic islet responses to glucose. *Cell Metab.* **24**, 389–401 (2016).
18. Wojtusciszyn, A., Armanet, M., Morel, P., Berney, T. & Bosco, D. Insulin secretion from human beta cells is heterogeneous and dependent on cell-to-cell contacts. *Diabetologia* **51**, 1843–1852 (2008).
19. Gaisano, H. Y., MacDonald, P. E. & Vranic, M. Glucagon secretion and signaling in the development of diabetes. *Front. Physiol.* **3**, 349 (2012).
20. Hauge-Evans, A. C. et al. Somatostatin secreted by islet δ-cells fulfills multiple roles as a paracrine regulator of islet function. *Diabetes* **58**, 403–411 (2009).
21. Koh, D.-S., Cho, J.-H. & Chen, L. Paracrine interactions within islets of Langerhans. *J. Mol. Neurosci.* **48**, 429–440 (2012).
22. Takahashi, N., Kishimoto, T., Nemoto, T., Kadowaki, T. & Kasai, H. Fusion pore dynamics and insulin granule exocytosis in the pancreatic islet. *Science* **297**, 1349–1352 (2002).
23. Low, J. T. et al. Insulin secretion from beta cells in intact mouse islets is targeted towards the vasculature. *Diabetologia* **57**, 1655–1663 (2014).
24. Wang, Y. et al. An optical method to evaluate both mass and functional competence of pancreatic α- and β-cells. *J. Cell Sci.* **129**, 2462–2471 (2016).
25. Grodsky, G. M. A threshold distribution hypothesis for packet storage of insulin and its mathematical modeling. *J. Clin. Invest.* **51**, 2047–2059 (1972).
26. Henquin, J. C., Nenquin, M., Stiernet, P. & Ahren, B. In vivo and in vitro glucose-induced biphasic insulin secretion in the mouse: pattern and role of cytoplasmic Ca^{2+} and amplification signals in β-cells. *Diabetes* **55**, 441–451 (2006).

27. Gini, C. Measurement of inequality of incomes. *Econ. J.* **31**, 124–125 (1921).
28. Zhang, J. et al. Red- and far-red-emitting zinc probes with minimal phototoxicity for multiplexed recording of orchestrated insulin secretion. *Angew. Chem. Int. Ed.* **60**, 25846–25855 (2021).
29. Kravets, V. et al. Functional architecture of pancreatic islets identifies a population of first responder cells that drive the first-phase calcium response. *PLoS Biol.* **20**, e3001761 (2022).
30. Singh, V. et al. Somatostatin receptor subtype-2-deficient mice with diet-induced obesity have hyperglycemia, nonfasting hyperglucagonemia, and decreased hepatic glycogen deposition. *Endocrinology* **148**, 3887–3899 (2007).
31. Huising, M. O., van der Meulen, T., Huang, J. L., Pourhosseinzadeh, M. S. & Noguchi, G. M. The difference δ-cells make in glucose control. *Physiology (Bethesda)* **33**, 403–411 (2018).
32. He, S. et al. The discovery of MK-4256, a potent SSTR3 antagonist as a potential treatment of type 2 diabetes. *ACS Med. Chem. Lett.* **3**, 484–489 (2012).
33. DiGruccio, M. R. et al. Comprehensive alpha, beta and delta cell transcriptomes reveal that ghrelin selectively activates delta cells and promotes somatostatin release from pancreatic islets. *Mol. Metab.* **5**, 449–458 (2016).
34. Zhang, Y. et al. Glucagon potentiates insulin secretion via β-cell GCGR at physiological concentrations of glucose. *Cells* **10**, 2495 (2021).
35. Svendsen, B. et al. Insulin secretion depends on intra-islet glucagon signaling. *Cell Rep.* **25**, 1127–1134 (2018).
36. Rutter, G. A., Ninov, N., Salem, V. & Hodson, D. J. Comment on Satin et al. "Take me to your leader": an electrophysiological appraisal of the role of hub cells in pancreatic islets. *Diabetes* **69**, 830–836 (2020). *Diabetes* **69**, e10–e11 (2020).
37. Satin, L. S., Zhang, Q. & Rorsman, P. "Take me to your leader": an electrophysiological appraisal of the role of hub cells in pancreatic islets. *Diabetes* **69**, 830–836 (2020).
38. Kravets, V., Dwulet, J. M., Schleicher, W. E., Piscopio, R. A. & Benninger, R. K. P. Beta cells subpopulations: do they control islet function? *Diabetologia* **62**, S133–S134 (2019).
39. van der Meulen, T. et al. Urocortin3 mediates somatostatin-dependent negative feedback control of insulin secretion. *Nat. Med.* **21**, 769–776 (2015).
40. Li, Q. et al. A cullin 4B-RING E3 ligase complex fine-tunes pancreatic δ cell paracrine interactions. *J. Clin. Invest.* **127**, 2631–2646 (2017).
41. Kellard, J. A. et al. Reduced somatostatin signalling leads to hypersecretion of glucagon in mice fed a high-fat diet. *Mol. Metab.* **40**, 101021 (2020).
42. Michael, D. J., Ritzel, R. A., Haataja, L. & Chow, R. H. Pancreatic β-cells secrete insulin in fast- and slow-release forms. *Diabetes* **55**, 600–607 (2006).
43. Li, D. et al. Imaging dynamic insulin release using a fluorescent zinc indicator for monitoring induced exocytotic release (ZIMIR). *Proc. Natl Acad. Sci. USA* **108**, 21063–21068 (2011).
44. Rorsman, P. et al. The cell physiology of biphasic insulin secretion. *News Physiol. Sci.* **15**, 72–77 (2000).
45. Yuan, T., Lu, J., Zhang, J., Zhang, Y. & Chen, L. Spatiotemporal detection and analysis of exocytosis reveal fusion "hotspots" organized by the cytoskeleton in endocrine cells. *Biophys. J.* **108**, 251–260 (2015).
46. Li, X. et al. Real-time denoising enables high-sensitivity fluorescence time-lapse imaging beyond the shot-noise limit. *Nat. Biotechnol.* **41**, 282–292 (2023).

Acknowledgements

This work was supported by the National Natural Science Foundation of China (81925022, 92054301, 92150301, T2288102, 91750203, 61827825, 12090053, 32088101, 32227802 and 32271235), the National Key Research and Development Program of China (2022YFC3400600, 2021YFA1101304, 2018YFA0900700, 2021YFF1200500 and 2020YFA0908200), Beijing Natural Science Foundation Key Research Topics (Z20J00059), the Fundamental Research Funds for the Central Universities (PKU2023XGK005, PKU2023LCXQ025) and the High-Performance Computing Platform of Peking University. L.C. was supported by New Cornerstone Science Foundation. X.P. was supported by the Postdoctoral Fellowship of Peking-Tsinghua Center for Life Sciences. H.R. was supported by the Boya Postdoctoral Fellowship of Peking University. We thank X. Yu (Shandong University) for the gift of the *Stdt* mouse. We thank K. Ouyang for advice on the experiments and the manuscript. We thank W. Ji for his help with the microscopy operation. We thank Z. Luo for help with data analysis.

Author contributions

L.C. and H. Liu conceived and supervised the study. X.P. designed and performed experiments, image processing, and data analysis and interpretation. H.R. performed mathematical analyses and interpretation with the guidance of C.T. L.Y. performed experiments, image processing and data analysis. S.T. participated in experiments related to disease research and in image processing. R.Z. designed the perfusion apparatus. Yunxiang Wu, Z.C. and J.Z. developed the red zinc probe. L.W. participated in developing the 'zinc flicker' method. H. Long, Yongdeng Zhang, Yi Wu, J.S., G.Q and J.W. developed the software platform for fusion event identification and image processing. T.X. contributed to developing the zinc flicker method and the semi-automatic software platform. C.H., Yulin Zhang, M.Z. and Yiwen Zhao participated in mouse management and physiological experiments. L.C. and X.P. wrote the paper, with contributions from all authors.

Competing interests

L.C., X.P., L.Y. and L.W. have authorized a patent application based on the zinc flicker method used in this work.

Additional information

Extended data is available for this paper at https://doi.org/10.1038/s42255-023-00962-0.

Supplementary information The online version contains supplementary material available at https://doi.org/10.1038/s42255-023-00962-0.

Correspondence and requests for materials should be addressed to Huisheng Liu or Liangyi Chen.

Peer review information *Nature Metabolism* thanks the anonymous reviewers for their contribution to the peer review of this work. Primary Handling Editor: Christoph Schmitt, in collaboration with the *Nature Metabolism* team.

[1]New Cornerstone Science Laboratory, National Biomedical Imaging Center, State Key Laboratory of Membrane Biology, Beijing Key Laboratory of Cardiometabolic Molecular Medicine, Institute of Molecular Medicine, School of Future Technology, Center for Life Sciences, Peking University, Beijing, China. [2]Department of Physiology and Pathophysiology, School of Basic Medical Sciences, Peking University, Beijing, China. [3]Bioland Laboratory, Guangzhou, China. [4]Center for Quantitative Biology and Peking-Tsinghua Center for Life Sciences, Academy for Advanced Interdisciplinary Studies, Peking University, Beijing, China. [5]The MOE Key Laboratory of Cell Proliferation and Differentiation, School of Life Sciences, Peking-Tsinghua Center for Life Sciences, Peking University, Beijing, China. [6]School of Life Sciences, Peking University, Beijing, China. [7]School of Software and Microelectronics, Peking University, Beijing, China. [8]Institute of Biophysics, Chinese Academy of Sciences, Beijing, China. [9]School of Life Sciences, Westlake University, Hangzhou, China. [10]Guangzhou National Laboratory, Guangzhou, China. [11]School of Biomedical Engineering, Guangzhou Medical University, Guangzhou, China. [12]National Biomedical Imaging Center, Beijing Key Laboratory of Cardiometabolic Molecular Medicine, Institute of Molecular Medicine, School of Future Technology, Center for Life Sciences, Peking University, Beijing, China. [13]PKU-IDG/McGovern Institute for Brain Research, Beijing, China. [14]These authors contributed equally: Xiaohong Peng, Huixia Ren, Lu Yang, Shiyan Tong. ✉e-mail: liu_huisheng@grmh-gdl.cn; lychen@pku.edu.cn

https://doi.org/10.1038/s42255-023-00962-0

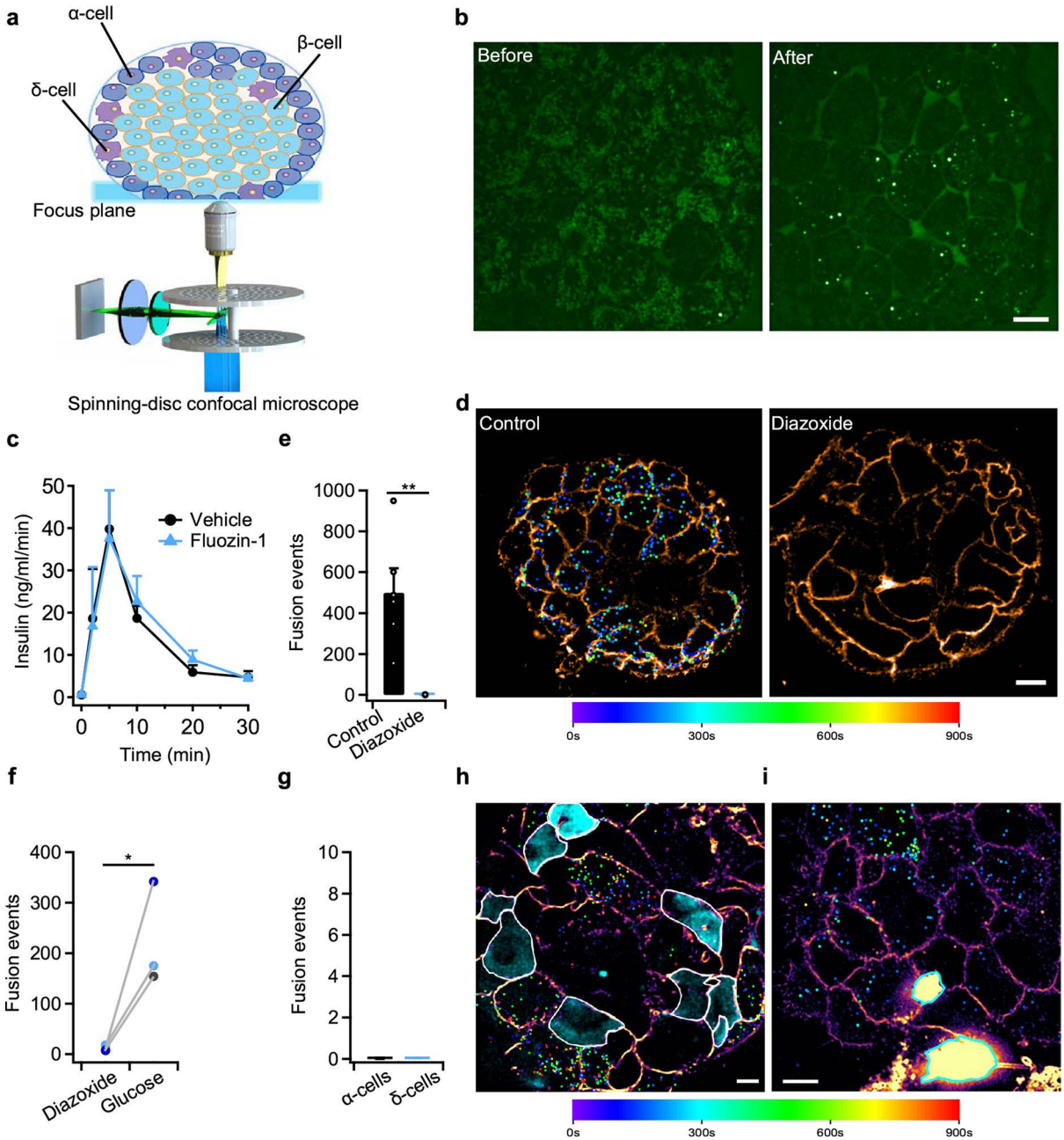

Extended Data Fig. 1 | Visualization of zinc flickers by spinning-disc confocal microscopy. a, Schematic diagram of imaging Zn^{2+}/insulin corelease ('Zinc flicker') with spinning-disc confocal microscope. The islet was seeded on a glass coverslip, and only a thin region above the glass coverslip (~1 μm) was imaged. **b**, Typical images of fusion events in the islet (from a male mouse) before and after stimulation with 18.2 mM glucose for 3 min. White puncta represented fused insulin granules labeled with fluorescent FluoZin-1. **c**, Dynamic insulin secretion evoked by 20 mM glucose with or without FluoZin-1 dye as determined by ELISA. Data were quantified from four independent experiments from male mice. **d**, Representative images of secretion (all fusion events in 15 minutes) in islets (from male mice) exposed to 11 mM glucose, either in the absence (Control) or presence of 250 μM diazoxide (Diazoxide). **e**, Averaged fusion events stimulated by 11 mM glucose (Control, n = 6 islets from 3 male mice) or with 250 μM diazoxide (Diazoxide, n = 5 islets from 3 male mice). **f**, Fusion events before (Diazoxide) and after (glucose) removal of diazoxide treatment on the same islet. n = 3 islets from 2 male mice. Significance was evaluated by ratio paired t test. **g**, Averaged fusion events detected in α-cells (n = 45 cells from 10 male islets) and δ−cells (n = 45 cells from 11 islets, mixed from male and female mice). **h-i**, Representative images of secretion (15 minutes) in male Glu-GCaMP (h) and Stdt islets (i) exposed to 18.2 mM glucose. White and cyan circles represented α and δ cells respectively. Cell membrane was coded by mpl-inferno color. Data was expressed as mean ± s.e.m. in c, e, g, and analyzed by two-sided unpaired Student t-test, * $p < 0.05$, ** $p < 0.01$. Scale bar = 10 μm.

https://doi.org/10.1038/s42255-023-00962-0

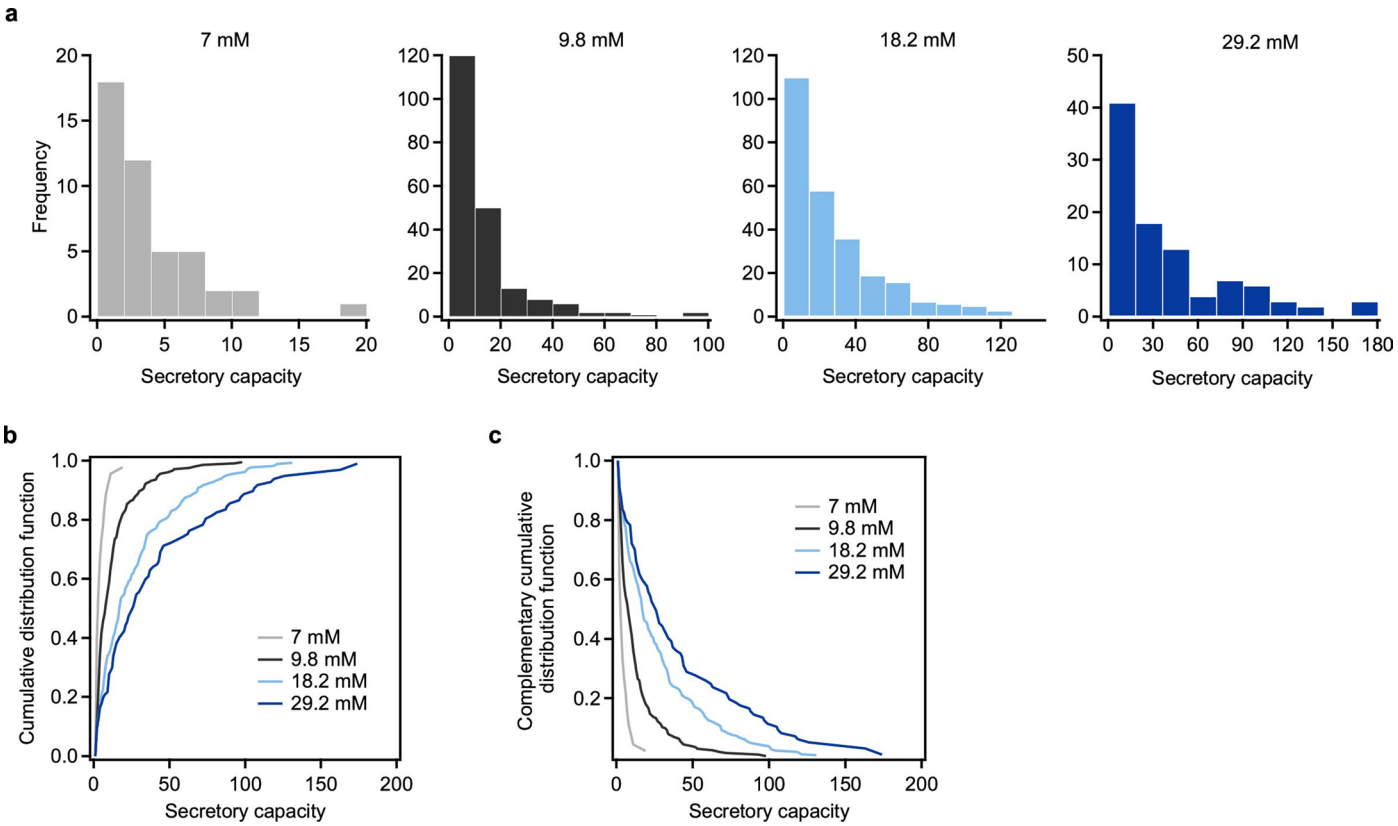

Extended Data Fig. 2 | The complementary cumulative distribution function of responsive cells under variable glucose stimulation. a, Frequency histograms of secretory capacity in responsive cells under different glucose stimulation. **b-c**, Cumulative distribution function (CDF, b) and complementary cumulative distribution function (CCDF, c) of secretory capacity under different glucose stimulation. For datasets, 7 mM, 45 cells; 9.8 mM, 204 cells; 18.2 mM, 261 cells and 29.2 mM, 97 cells, respectively.

https://doi.org/10.1038/s42255-023-00962-0

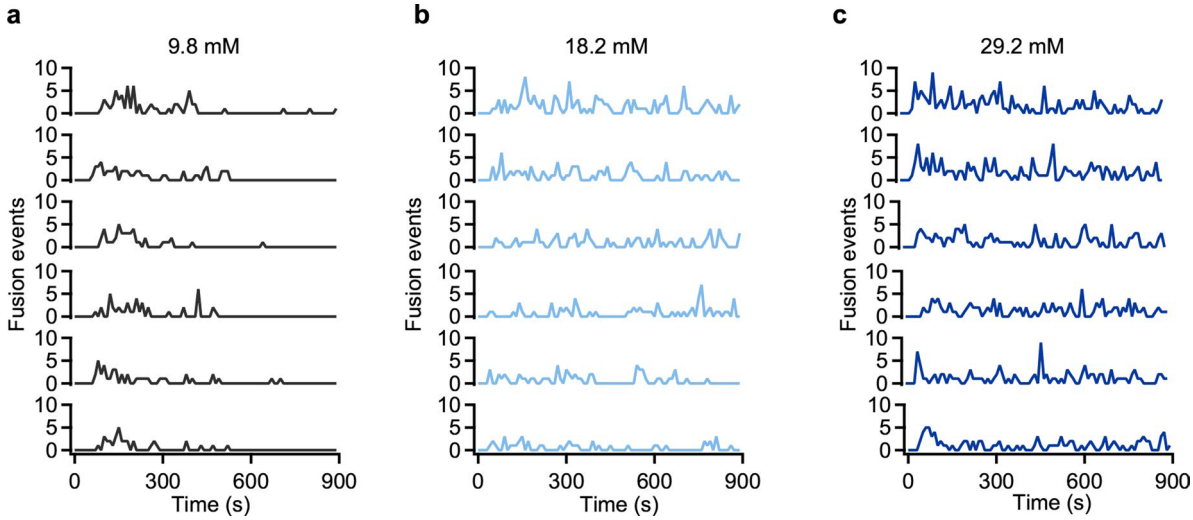

Extended Data Fig. 3 | The synchronization of RRβ cells under variable glucose stimulation. a–c, Exocytosis frequency histograms of fusion events from the top six cells stimulated by 9.8 mM (a, male), 18.2 mM (b, male) and 29.2 mM (c, male) glucose.

https://doi.org/10.1038/s42255-023-00962-0

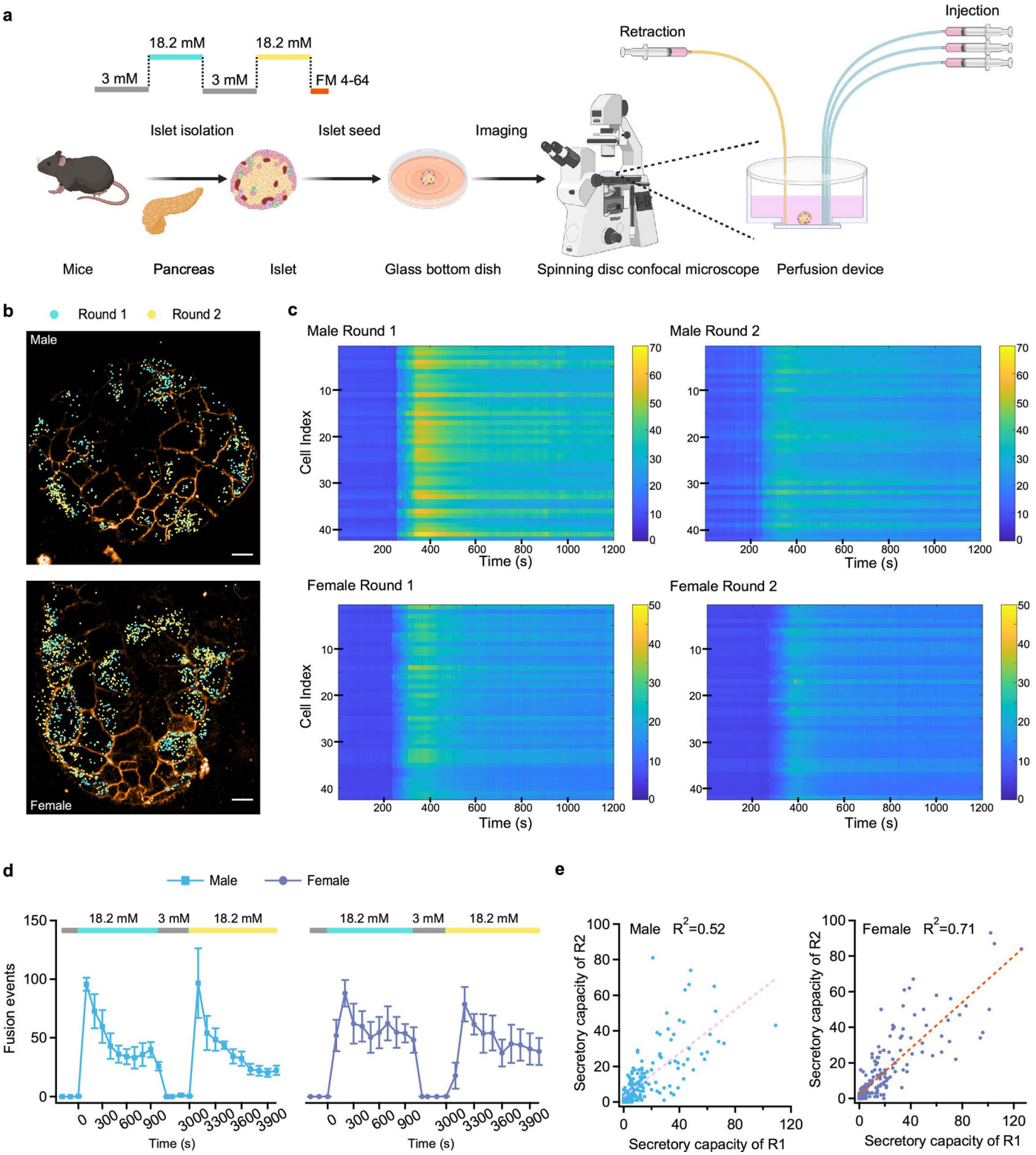

Extended Data Fig. 4 | Repeated perfusion-stimulated exocytosis in mouse islets. a, A schematic illustration of the perfusion apparatus and corresponding experimental procedure. Created with BioRender.com. **b**, Representative illustrations of insulin secretion in male and female islets under continuous perfusion stimulation. **c**, Heatmaps showcasing the β-cell Ca2+ dynamics within male and female islets undergoing intermittent 18.2 mM glucose stimulations. The color-bar indicates the fluorescent intensity within the islets. Each row represents individual β-cells within a singular islet. The x-axis represents the timeframe subsequent to glucose stimulation. **d**. Time-dependent fusion events in male and female islets triggered by recurring stimulation with 18.2 mM glucose. Male, n = 6 islets from 4 mice; female, n = 5 islets from 4 mice. Data was expressed as mean ± s.e.m. **e**. Correlations between the secretory capacity observed during two separate glucose stimulations. Scale bar = 10 μm.

https://doi.org/10.1038/s42255-023-00962-0

a

	1st responder	2nd follower	Leader cells	Hub cells	RRβ cells
Steady second phase	18	18	NaN	NaN	81
Oscillating second phase	6	6	6	7	26
Colocalization with RRβ in steady	61%	17%	NaN	NaN	/
Colocalization with RRβ in oscillatir	67%	33%	67%	29%	/

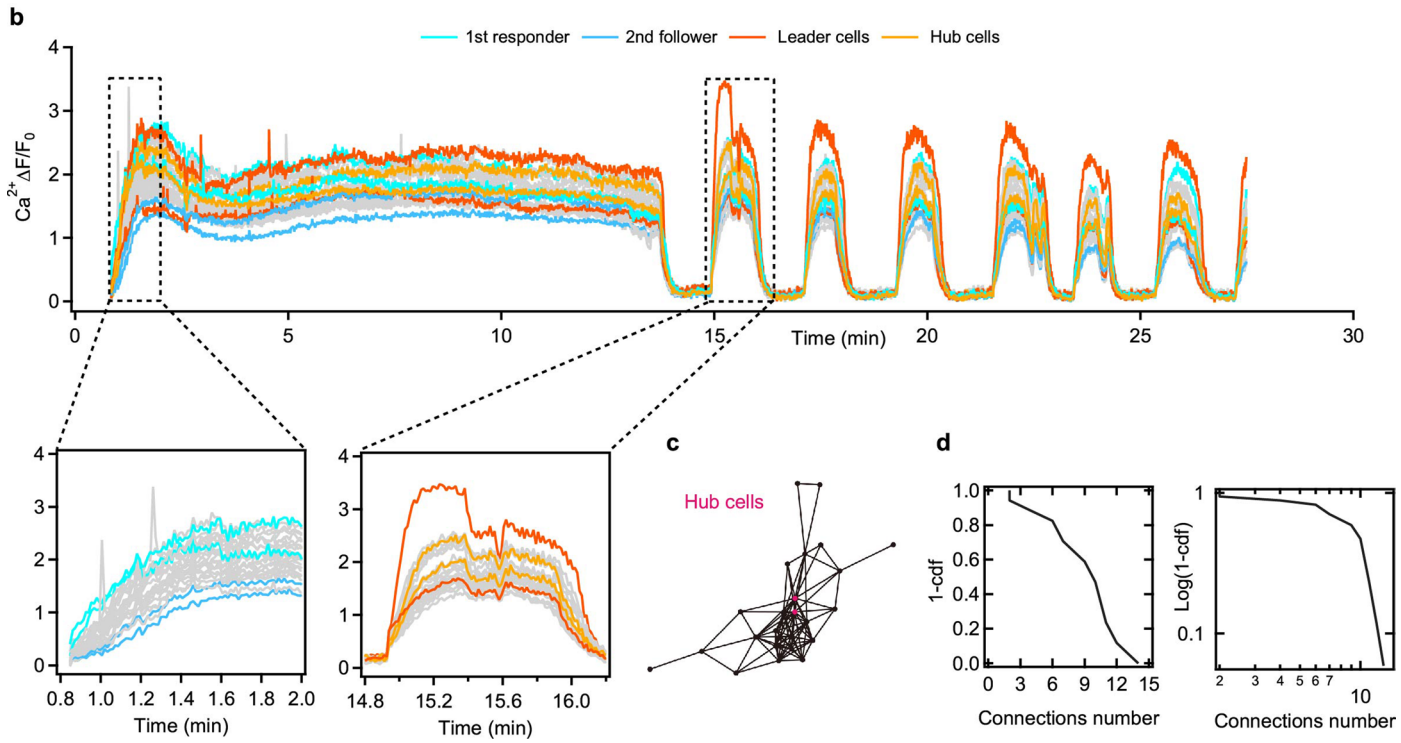

Extended Data Fig. 5 | Comparison of the secretory capacity of specific cell types with RRβ cells. a, The proportion of various cell types classified based on their Ca2+ dynamics in relation to RRβ cells. **b**, The definition of 1st responder cells and 2nd follower cells, along with hub cells and leader cells. The left box presents the 1st responders and second responders; the right box portrays hub cells and leader cells. **c**, A representative functional connectivity map in a single male islet, with red dots symbolizing the hub cells. **d**, The distribution of connection numbers for different cells within an islet; the right panel depicts the log-log plot shown on the left panel. The current plot indicates that the Ca2+ connectivity map does not follow the power law distribution, which would be represented as an inverse linear relationship within the log-log plot.

https://doi.org/10.1038/s42255-023-00962-0

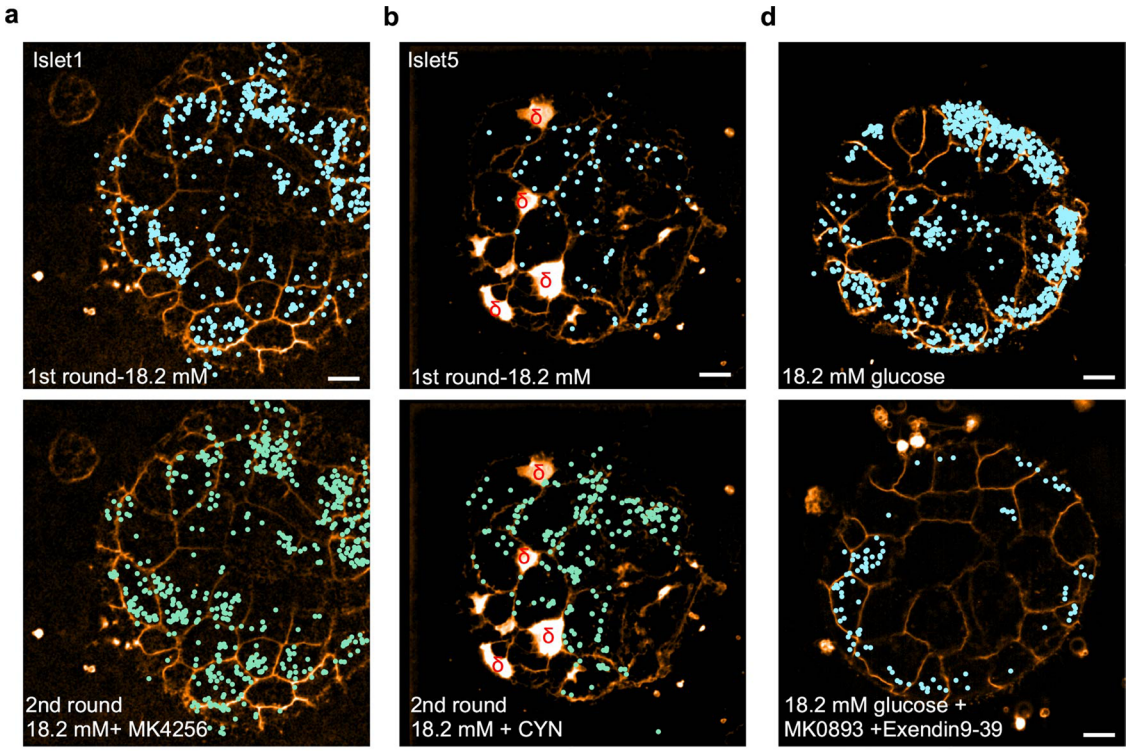

c

Islet ID	Treatment	δ cells in volume	δ cells in plane	Secretion of R1	Secretion of R2
Islet 1	MK 4256	1	0	583	596
Islet 2	MK 4256	2	1	749	276
Islet 3	MK 4256	16	7	12	9
Islet 4	CYN	6	2	84	202
Islet 5	CYN	8	4	65	236
Islet 6	CYN	22	5	0	0
Islet 7	CYN	10	9	113	26

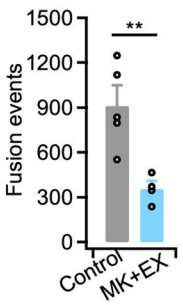

Extended Data Fig. 6 | Both δ- and α- cell influence β-cell secretion with the islet. a. A representative example of fusion events from islet 1 in c, during the initial round of glucose stimulation and the subsequent round with 10 nM MK4256. **b**, A representative example of fusion events from islet 5 in c, during the initial round of glucose stimulation and the second round with 200 nM CYN 154806. **c**, A tabular representation detailing fusion events from islets treated with either of the SSTR antagonists. Islet 3 isolated from male mouse, and other islets isolated from female mice. **d**, A typical example of insulin granule fusion evoked by 18.2 mM glucose (upper, male) or with 1 μM MK0893 and 1 μM Exendin9-39 (down, male). **e**, Total number of fusion events evoked by 18.2 mM glucose (Control, n = 5 islets from 3 male mice) or with 1 μM MK0893 and 1 μM Exendin9-39 (MK+Ex, n = 4 islets from 3 male mice). Data was expressed as mean ± s.e.m. and analyzed by two-sided unpaired Student t-test, ** $p < 0.01$.

https://doi.org/10.1038/s42255-023-00962-0

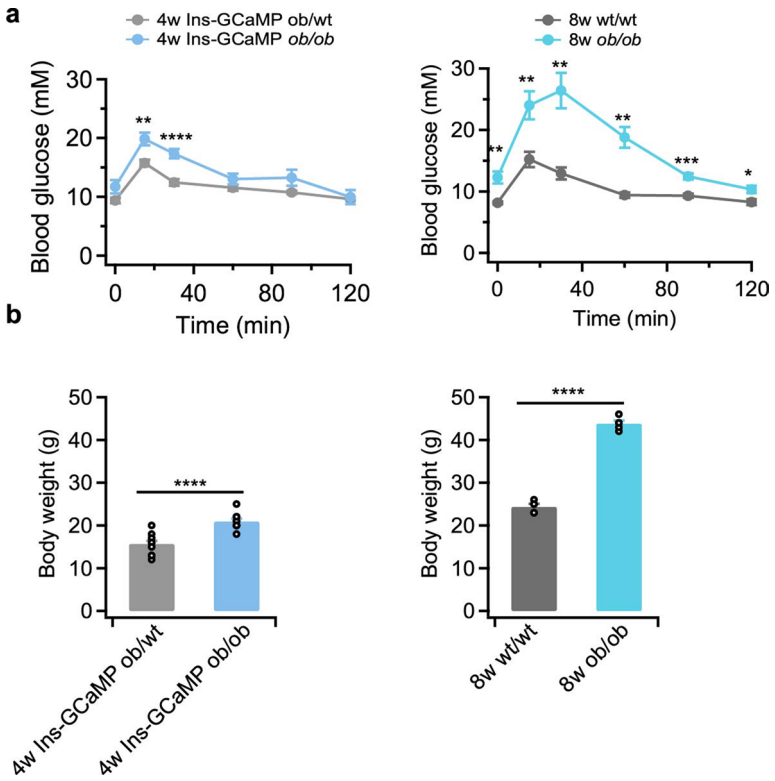

Extended Data Fig. 7 | Physiology phenotypes of 4-week and 8-week ob/ob mice. a, b, The glucose tolerance test (a) and body weight (b) of 4w and 8w ob/ob mice and their littermates. n = 12 mice (6 male and 6 female) from 4w Ins-GCaMP ob/wt mice, 10 mice (5 male and 5 female) from 4w Ins-GCaMP ob/ob mice, 5 male mice from 8w wt/wt and 5 male mice from 8w ob/ob mice. Data was expressed as mean ± s.e.m., p values were analyzed by two-sided unpaired Student's t-tests, *p < 0.05, ** p < 0.01, *** p < 0.001, **** p < 0.0001.

https://doi.org/10.1038/s42255-023-00962-0

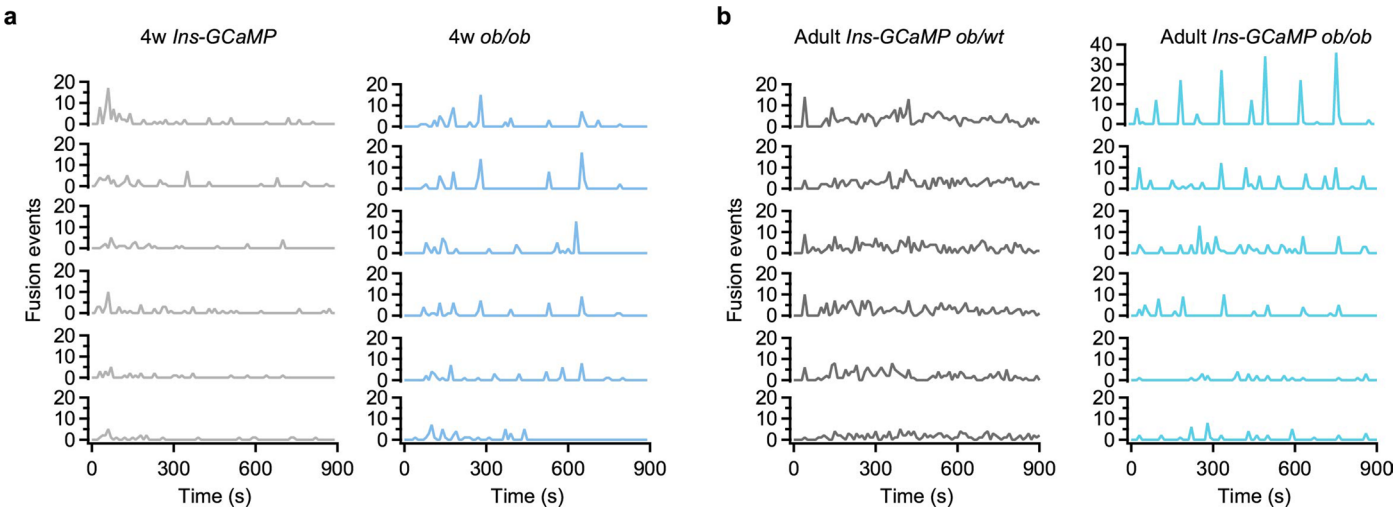

Extended Data Fig. 8 | The synchronization of RRβ cells within ob/ob islets. **a**, Exocytosis frequency histograms of fusion events from the top six RRβ cells in 4-week Ins-GCaMP (left, male) and ob/ob islets (right, male). **b**, Exocytosis frequency histograms of fusion events from the top six RRβ cells in adult Ins-GCaMP ob/wt (left, male) and Ins-GCaMP ob/ob islets (right, female).

nature portfolio

Corresponding author(s): Liangyi Chen

Last updated by author(s): Nov 3, 2023

Reporting Summary

Nature Portfolio wishes to improve the reproducibility of the work that we publish. This form provides structure for consistency and transparency in reporting. For further information on Nature Portfolio policies, see our Editorial Policies and the Editorial Policy Checklist.

Statistics

For all statistical analyses, confirm that the following items are present in the figure legend, table legend, main text, or Methods section.

n/a	Confirmed	
☐	☒	The exact sample size (*n*) for each experimental group/condition, given as a discrete number and unit of measurement
☐	☒	A statement on whether measurements were taken from distinct samples or whether the same sample was measured repeatedly
☐	☒	The statistical test(s) used AND whether they are one- or two-sided *Only common tests should be described solely by name; describe more complex techniques in the Methods section.*
☒	☐	A description of all covariates tested
☐	☒	A description of any assumptions or corrections, such as tests of normality and adjustment for multiple comparisons
☐	☒	A full description of the statistical parameters including central tendency (e.g. means) or other basic estimates (e.g. regression coefficient) AND variation (e.g. standard deviation) or associated estimates of uncertainty (e.g. confidence intervals)
☐	☒	For null hypothesis testing, the test statistic (e.g. *F*, *t*, *r*) with confidence intervals, effect sizes, degrees of freedom and *P* value noted *Give P values as exact values whenever suitable.*
☒	☐	For Bayesian analysis, information on the choice of priors and Markov chain Monte Carlo settings
☒	☐	For hierarchical and complex designs, identification of the appropriate level for tests and full reporting of outcomes
☒	☐	Estimates of effect sizes (e.g. Cohen's *d*, Pearson's *r*), indicating how they were calculated

Our web collection on statistics for biologists contains articles on many of the points above.

Software and code

Policy information about availability of computer code

Data collection	All images were acquired with a spinning-disc confocal microscope based on a CSU-X1 Yokogawa head mounted on an inverted IX-81 Olympus microscope equipped with a X100 (NA1.30, Olympus) or X60 (NA1.35, Olympus) oil immersion objective lens. The images were captured either by an electron-multiplying charge-coupled device (EMCCD) camera (Andor iXon3 897) or an s-CMOS camera (C14440-20UP, Hamamatsu, Japan). All the devices were controlled by MetaMorph software v7.8.1.0 (Molecular Devices). Insulin secretion was measured by commercial ELISA kit (Millipore, EZRMI-13K).
Data analysis	Images were pre-processed by Image J2 (Fiji,v1.53t) or our lab published Sparse-SIM algorithm (https://doi.org/10.1038/s41587-021-01092-2). Fusion events were detected by our previously published algorithm (https://doi.org/10.1016/j.bpj.2014.11.3462) or TrackMate (v7.9) in Image J2, detail procedure are described in Methods section. Other analysis (such as Gini coefficient, Voronoi diagram, synchronization, et.al) were performed by Matlab2021a, corresponding functions and algorithm are described in the Methods section in detail. MatLab codes are also available from the corresponding authors upon request. Statistical analysis was performed by IGOR Pro 8.0 (WaveMetrics, Portland, OR, USA)y.

For manuscripts utilizing custom algorithms or software that are central to the research but not yet described in published literature, software must be made available to editors and reviewers. We strongly encourage code deposition in a community repository (e.g. GitHub). See the Nature Portfolio guidelines for submitting code & software for further information.

Data

Policy information about availability of data

All manuscripts must include a data availability statement. This statement should provide the following information, where applicable:

- Accession codes, unique identifiers, or web links for publicly available datasets
- A description of any restrictions on data availability
- For clinical datasets or third party data, please ensure that the statement adheres to our policy

All data supporting this study are provided in Source data files. As original images have some other information to analysis, we cannot upload all of them to public database now, instead of uploading some typical movies to show our signals, but. If someone interested, they are also available from corresponding author upon request.

Research involving human participants, their data, or biological material

Policy information about studies with human participants or human data. See also policy information about sex, gender (identity/presentation), and sexual orientation and race, ethnicity and racism.

Reporting on sex and gender	N/A.
Reporting on race, ethnicity, or other socially relevant groupings	N/A.
Population characteristics	N/A.
Recruitment	N/A.
Ethics oversight	N/A.

Note that full information on the approval of the study protocol must also be provided in the manuscript.

Field-specific reporting

Please select the one below that is the best fit for your research. If you are not sure, read the appropriate sections before making your selection.

☒ Life sciences ☐ Behavioural & social sciences ☐ Ecological, evolutionary & environmental sciences

For a reference copy of the document with all sections, see nature.com/documents/nr-reporting-summary-flat.pdf

Life sciences study design

All studies must disclose on these points even when the disclosure is negative.

Sample size	The sample sizes were determined according to those used in similar studies and justified by the power analyses. Under each condition, at least 3 islets and multiple animals were collected.
Data exclusions	Data was excluded when it was outliers or clearly technical issues were identified.
Replication	All independent experiments (n) were conducted at least triplicate. Most of conditions were repeated by more than three animals. And all main conclusions have been repeated by two experimenters independently.
Randomization	We picked up mice and islets randomly for imaging, and randomly allocated islets for different groups.
Blinding	There was no blinding for group allocation, but was blinding for data analysis. Data processors were usually blinded for the conditions of those data they were dealing with.

Reporting for specific materials, systems and methods

We require information from authors about some types of materials, experimental systems and methods used in many studies. Here, indicate whether each material, system or method listed is relevant to your study. If you are not sure if a list item applies to your research, read the appropriate section before selecting a response.

Materials & experimental systems

n/a	Involved in the study
☒	☐ Antibodies
☒	☐ Eukaryotic cell lines
☒	☐ Palaeontology and archaeology
☐	☒ Animals and other organisms
☒	☐ Clinical data
☒	☐ Dual use research of concern
☒	☐ Plants

Methods

n/a	Involved in the study
☒	☐ ChIP-seq
☒	☐ Flow cytometry
☒	☐ MRI-based neuroimaging

Animals and other research organisms

Policy information about studies involving animals; ARRIVE guidelines recommended for reporting animal research, and Sex and Gender in Research

Laboratory animals	Mice strains including Ins1-Cre-GCaMP6f, Sst-Cre-Tdt-tomato, Glu-Cre-GCaMP6f, C57BL/6N, ob/ob and Ins1-Cre-GCaMP6f ob/ob mice.C57BL/6N mice (aged 8~10 weeks) were purchased from the Beijing Vital River Laboratory Animal Technology Co., Ltd. (Beijing, China). 4w and 8w ob/ob mice were purchased from the GemPharmatech Co., Ltd. 2-4 month Stdt mice were a gift from Prof. Xiao Yu at Shandong University. 2-4month Ins-GCaMP mice were crossbred from the Ins1-Cre+ (Jackson Laboratories, stock number 026801) and GCaMP6f f/f lines (Jackson Laboratories, stock number 029626). 4w-8w Ins-GCaMP ob/ob mice were crossbred from Ins-GCaMP mice and ob/ob mice, and their littermates Ins-GCaMP ob/wt as control. 2-3 month Glu-GCaMP mice were crossbred by Glucagon Cre (kindly gifted by Prof. Herbert Y. Gaisano from the University of Toronto, Canada) and GCaMP6f lines. All mice used for experiments were bred on the C57BL/6 background and were maintained in an specific pathogen-free animal facility (SPF) of the Peking University. The facility was accredited by Association for Assessment and Accreditation of Laboratory Animal Care (AAALAC). Mice were housed at a 12 h light/ dark cycle with 22? temperature and 40%–60% humidity environment, free to access water and a chow diet.
Wild animals	This study did not involve wild animals.
Reporting on sex	we used both male and female mice for our findings.
Field-collected samples	This study did not involve samples collected from the field.
Ethics oversight	The studies were approved by the Ethics Committee of Peking University and performed at the animal facility of Peking University accredited by the Association for Assessment and Accreditation of Laboratory Animal Care International.

Note that full information on the approval of the study protocol must also be provided in the manuscript.